Research Square

Preprints are preliminary reports that have not undergone peer review.
They should not be considered conclusive, used to inform clinical practice,
or referenced by the media as validated information.

Direct microglia replacement reveals the impact of ontogeny on murine microglial responses to pathologic amyloid aggregation

Chet Huan Oon
University of Pennsylvania
Eli M Levitt
University of Pennsylvania
Daniel A Shapiro
University of Pennsylvania
Carleigh A O'Brien
University of Pennsylvania
Mara R Davis
University of Pennsylvania
Olga Shestova
University of Pennsylvania
Jessie Axsom
University of Pennsylvania
Fazeela Yaqoob
University of Pennsylvania
Vilija Lomeikaitė
VUGENE
Dimitrios Koumadorakis
VUGENE
Milda Milčiūtė
VUGENE
Edita Karosienė
VUGENE
Max Shestov
University of Pennsylvania
Ryan N Anderson
University of Pennsylvania
Ryan J Rahman
University of Pennsylvania
Sonia I Lombroso

University of California, San Francisco

Michael S Haney

University of Pennsylvania

Mariko L Bennett

Children's Hospital of Philadelphia

Saar Gill

University of Pennsylvania

F. Chris Bennett

frederick.bennett@pennmedicine.upenn.edu

University of Pennsylvania

Research Article

Keywords: microglia ontogeny, microglia replacement, Alzheimer's Disease, single-cell RNA sequencing, Disease-associated microglia (DAM)

Posted Date: September 23rd, 2026

DOI: https://doi.org/10.21203/rs.3.rs-10963419/v1

License: This work is licensed under a Creative Commons Attribution 4.0 International License. Read Full License

Additional Declarations: Competing interest reported. F.C.B. and M.L.B. are co-inventors on a patent filed by the board of trustees of the Leland Stanford Junior University (12612599), related to methods of microglia replacement. F.C.B. holds shares in Savanna Biotherapeutics, Inc. M.L.B. holds shares in Alector, Inc. L.V., D.K., M.M., and K.E. are employees of VUGENE.

Abstract

Microglia are central to the progression of many neurodegenerative diseases, especially Alzheimer's Disease (AD). Adoptive transfer of engineered cells has demonstrated clinical benefit in oncology, autoimmune disease, and inherited blood disorders. Replacement of disease-affected microglia thus holds high therapeutic potential in AD, but how microglia replacement, including the source and ontogeny of donor microglia surrogates, fundamentally impacts AD neuropathology, is unresolved. We recently developed a microglia replacement approach based on engineered, inhibitor resistant CSF1R variants, that we here deployed in the 5xFAD model to better understand how microglia replacement impacts neuropathology and associated cell states spurred by aggressive amyloid aggregation. We achieved near-complete, direct microglia replacement prior to plaque accumulation, using *ex vivo* expanded hematopoietic stem cells (HSCs), Hoxb8 conditionally immortalized macrophages, and primary CD11b+ cells from early postnatal brain as donor sources. Although two months after transplant, CD11b+ brain cells slightly increased plaque burden, and conditionally immortalized macrophages slightly decreased astrogliosis, microglia replacement did not otherwise impact plaque burden, astrogliosis, nor the transcriptional state of astrocytes and oligodendrocytes as measured by single-cell RNA sequencing in 5 month old mice. In stark contrast, we found that donor cell ontogeny highly impacted both homeostatic and amyloid reactive macrophage state. In particular, and unlike transplanted microglia, HSC and Hoxb8 donor populations adopted a disease associated microglia (DAM)-like baseline state, but upon amyloid challenge, failed to effectively induce the complete DAM signature. Overall, these findings reveal large differences in the response of fetal origin compared with adult bone marrow-derived microglia to neuropathology, but that these large differences do not have a commensurate impact on the brain environment, important considerations for the development of microglia replacement therapies and the study of brain myeloid cell infiltration.

BACKGROUND

Microglia play substantial causal roles in AD pathobiology and treatment, as supported by human genetics studies implicating microglial genes in disease risk [1–8], model systems demonstrating impacts on hallmark neuropathology [9–15], and their contribution to the therapeutic effects of amyloid immunotherapies [16–18]. However, precise microglial contributions to AD have been challenging to pinpoint, in large part because microglia, and their roles in AD, are highly plastic. Universally, microglia undergo dramatic state changes in response to their environment [19]. In AD, this unfolds in highly spatially confined domains, for example around amyloid plaques [20], presenting many experimental challenges. In addition, the contribution of microglia to AD varies across disease course (helpful early, harmful late) and pathology (amyloid vs. tau) [21], all complicated by the likelihood that in humans, microglia are likely replaced by infiltrating monocytes from the circulation that may be both helpful and harmful themselves [22–23]. Altogether, these challenges highlight the need for new tools to manipulate and study dynamic bidirectional relationships between brain parenchymal macrophages and their environment.

Microglia replacement - the depletion of endogenous microglia, followed by adoptive transfer of macrophage surrogates that engraft the brain in their place [24], enables the study of these complex dynamics. We recently developed new microglia replacement methods, where donor cells are directly injected into the CNS, offering the opportunity to compare how defined donor cell populations, including engineered microglia surrogates, respond to the healthy and diseased brain environments, and in turn how they affect neural cells and tissues [25–26]. In this manuscript, we expand the scope and potential of microglia replacement, using stereotaxic injection to directly engraft engineered murine CSF1R inhibitor resistant macrophages into the WT and 5xFAD brain, to assess how different donor macrophage types respond to pathologic amyloid accumulation, and its consequences. We set out to answer two main questions: 1) How does microglia replacement impact amyloid-driven neuropathology and glial cell responses and 2) How much does donor cell source and ontogeny modify these responses? We found that CSF1R inhibitor treatment and microglia replacement prior to plaque accumulation do not substantially impact early amyloid pathology in the 5xFAD model. Using single-cell transcriptomics to create an atlas of microglia replacement, we found that donor macrophages of differing ontogeny have different responses to pathology, and that only true, fetal origin microglia could dynamically regulate the disease-associated macrophage (DAM) transcriptional program. Yet, neither microglia replacement nor depletion appreciably affected astrocyte and oligodendroglial-lineage cell states in our assays, regardless of donor macrophage type. These findings establish a new microglia replacement platform for research and therapy development in AD, and enrich our understanding of the unique properties of tissue resident macrophages.

RESULTS

Microglia depletion with the CSF1R antagonist PLX3397 and transplantation of inhibitor-resistant CSF1R ^{G793A} donor cells enables robust microglia replacement in adult WT and 5xFAD mice

To investigate how donor cell type and a diseased brain environment impact microglia replacement, we developed a microglia depletion and transplantation paradigm for adult 5xFAD mice, a model of aggressive amyloid deposition [27]. We used the CSF1R inhibitor PLX3397 (PLX) to deplete microglia, and then delivered donor cell surrogates from a transgenic mouse expressing the PLX inhibitor resistant CSF1R^{G793A} variant (Fig. 1A) [28–29]. We compared three donor cell populations: *ex vivo* expanded hematopoietic stem and progenitor cells (exHSPC) [29–31], Hoxb8 conditionally immortalized myeloid progenitors (Hoxb8) [32–33], and primary CD11b+ cells from the early postnatal brain (CD11b + Br). Donor cells were distinguished from CD45.2 host cells by expression of either one (Hoxb8) or two (exHSPC and CD11b + Br) alleles of the congenic marker CD45.1. We depleted host microglia continuously using 600 mg/kg PLX3397 chow from 7 weeks of age, prior to significant plaque accumulation. At eight weeks, we delivered donor cells by hippocampus-targeted stereotaxic injection, then harvested at 4.5–5 months of age, after amyloid pathology is well-established [27, 34].

To assess engraftment efficiency of the transplant paradigm, we performed flow cytometry analysis of brain immune cells, distinguishing CD45.1 donor from CD45.2 host cells to measure donor cell

chimerism (Fig. 1B). As expected, CD11b+ cells were host-derived in untreated WT and 5xFAD animals, and PLX treatment eliminated endogenous CD11b+ cells. In contrast, nearly all CD11b+ cells were donor-derived in animals transplanted with exHSPC, Hoxb8, and CD11b+ brain cells (Fig. 1B-B'**, S1A, S1B**), demonstrating near complete replacement of the host microglial compartment using this paradigm. While all engrafted donor cells expressed TMEM119 protein, a marker of parenchymal engraftment (Fig. 1B), exHSPC- and Hoxb8-transplanted brains showed reduced MFI (**Figure S1C**), as previously noted following transplantation [29, 33, 35].

To confirm that donor cells repopulated the parenchyma, we performed IBA1 immunohistochemistry and quantified donor cell distribution across coronal sections. While control PLX-treated brains lacked IBA1 + cells, those transplanted with each of the 3 donor cell types showed comparable percent area coverage to untreated WT and 5xFAD controls (Fig. 1C-C'). In WT, all three donor cell types adopted a microglia-like morphology and restored IBA1 + area and density in the hippocampus and dorsal subiculum to that of control (Fig. 1D-E'). In 4–6 month old 5xFAD mice in our colony, amyloid deposition is sparse in the cortex and hippocampus, but dense in the dorsal subiculum (**Figure S1D**). In the hippocampus of 5xFAD mice, the area coverage and density of IBA1 + microglia and their morphology were comparable in transplanted and untreated mice, regardless of host genotype. (Fig. 1D-D'). In the dorsal subiculum where plaque burden is high, findings diverged across donor cell types (Fig. 1E-E'). Though all donor cell types engaged amyloid plaques and had increased density compared to those in WT hosts, they engaged plaques less, adopted a less hypertrophic appearance, had significantly lower IBA1 + area coverage, and absolute cell density than endogenous microglia. As previously reported, PLX treatment spared a small population of plaque-associated microglia (Fig. 1E) [12]. Together, these results demonstrate that intracranial transplantation of multiple CSF1R^{G793A} cell types with microglia surrogate potential leads to robust microglia replacement.

Microglia replacement has minimal impact on early amyloid burden and reactive astrogliosis in the 5xFAD model

Having established robust microglia replacement across all donor sources and hosts (Fig. 1), we asked whether cell injection and donor origin influence amyloid pathology. We first quantified amyloid plaque burden by 6E10 immunostaining in the 5xFAD subiculum across untreated, PLX-treated, and transplanted conditions (Fig. 2A-A'). While PLX treatment, exHSPC transplant, and Hoxb8 transplant did not significantly alter plaque burden compared to untreated 5xFAD controls, CD11b + Br-transplanted animals showed a small, statistically significant increase in plaque area.

To assess whether this difference in amyloid burden could relate to differences in lysosomal abundance, we performed CD68 immunostaining and quantified CD68 + area across untreated, PLX depleted, and transplanted conditions in WT and 5xFAD subiculum (Fig. 2B-B'). In WT subiculum, CD68 area did not differ significantly across conditions. In 5xFAD subiculum, CD68 area was increased compared to WT in all conditions, but was lower in all three transplanted groups than untreated 5xFAD control. We found a

similar pattern for IBA1 percent area, leading to a CD68/IBA1 ratio that did not significantly differ across conditions.

Reactive astrogliosis is an AD hallmark regulated by microglial inflammatory signals [37]. We compared GFAP immunoreactivity in the dorsal subiculum across all transplant and control conditions (Fig. 2C-C'). As in a prior study, microglia replacement did not substantially impact GFAP area in WT hosts [36]. In all conditions, GFAP was increased in 5xFAD relative to WT controls but was slightly lower in PLX-treated and donor-transplanted 5xFAD animals than untreated 5xFAD, a decrease statistically significant only for Hoxb8 transplanted animals, which had the lowest percent GFAP area. In summary, although donor cell populations differed from endogenous microglia in terms of morphology and plaque association, this only mildly influenced astrocyte reactivity, and did not substantially alter amyloid burden.

Generation of a single cell transcriptional atlas of microglia replacement in WT and 5xFAD hosts.

To assess how engrafted donor cells respond to brain environmental signals, and how microglia replacement alters other brain cells, we used single cell RNAseq to profile the cortex and hippocampus of WT and 5xFAD mice that had undergone microglia depletion and replacement from primary CD11b+ brain cells, exHSPC or Hoxb8 sources, including untreated and PLX only controls for both host genotypes (n = 31 total independent replicates, with 3–4 individual mice per group; Fig. 3A). We applied an established, papain-based isolation method that includes transcriptional and translational inhibitors, and used 10x based sequencing, to profile all CNS cell types, including transplanted microglia surrogates [38–40]. Following quality control (**Figure S2A**), 150,899 total cells remained for downstream analysis (Fig. 3B), represented across all ten experimental groups (**Figure S2B, Supplementary Table 1**). Marker-based cluster annotation identified expected CNS cell populations, including astrocytes, oligodendrocytes, microglia, neurons, pericytes, vascular smooth muscle cells, and endothelial cells (Fig. 3C). In this study, we focused subsequent analyses on three cell types due to their known role in AD pathogenesis, and the presence of substantial cell numbers for each in our sequencing data: microglia/macrophages, astrocytes, and oligodendrocytes.

Transplanted microglia differ from endogenous in both WT and 5xFAD hosts

Focusing first on the myeloid lineage, we subclustered microglia/macrophages, excluding minor subclusters with uniformly low UMI that did not resolve stably from contaminating astrocyte-containing clusters, yielding 32,015 cells for subsequent analyses (Fig. 4A, S3A; **Methods**). Beyond the presence of a minor population of border associated macrophages (BAMs; **Figure S3B**), nearly all myeloid cells fell into one of two groups: those with a signature of embryonic lineage microglia, expressing all microglia markers, including *Sall1* and high *P2ry12* [35, 41–42]; and those with a signature of monocyte-derived microglia, expressing most microglia markers but lacking *Sall1*, and expressing monocyte-derived markers including *Ms4a7* and *Clec12a* (**Figure S3B**). We applied an existing, well-validated construct to define murine parenchymal macrophages of embryonic vs. HSC ontogeny by transcriptomic signature

[43], which uses the prefix em- to describe cells with the complete signature of embryonic origin microglia, and the prefix mo- to describe those with a monocyte-derived microglia signature (Fig. 4A). As expected, microglia generated from exHSPCs and Hoxb8s resided almost exclusively in mo-MG clusters, had slightly lower microglia identity gene-set scores, and higher HSC-lineage scores (Fig. 4B-B'). True endogenous microglia in untreated control animals clustered in the em-MG cluster, with high microglia identity scores, and low HSC-lineage scores. The transplanted CD11b+ brain cell group, where donor cells were isolated from early postnatal donor mouse brains by CD11b positive selection, generated parenchymal macrophages residing in both clusters (**Figure S3C, 4B-B'**). This most likely reflects our impure isolation strategy, which was necessary to obtain sufficient donor cell yield, but did not remove non-microglial macrophages from the fetal head. Though unplanned, this provided the opportunity for within-host comparison of transplanted em- and mo-MGs.

Embryonic (Em-) and monocyte-like lineage (mo-) clusters each contained three analogous microglial states–a small population expressing an interferon stimulated gene signature, a predominant homeostatic population, and a disease associated microglia (DAM) population, found only in 5xFAD hosts (Fig. 4B-B**', S3B, S3D**). Using principal components analysis (PCA), we plotted the pseudobulk profile of homeostatic and DAM clusters across each combination of donor cell type (endogenous MG, transplanted primary CD11b+ cells, exHSPC-derived, Hoxb8-derived microglia) and host genotype (WT, 5xFAD), noting that groups clustered together based on both ontogeny (em-MG vs mo-MG) and state (homeostatic vs DAM; Fig. 4C, S3E). When we compared homeostatic transplanted em- to mo-MGs in WT hosts, we found 2,292 significantly expressed genes, while exHSPC compared to Hoxb8-derived mo-MGs had only 373 (**Figure S3F, Supplementary Table 2**), demonstrating that donor source has less impact on MG gene expression than ontogeny. exHSPC-enriched genes included hematopoietic progenitor regulators (*Pbx1, Eng*), whereas Hoxb8-enriched genes included developmental transcription factors (*Six1, Eya4*) and lipid and iron handling genes (*Ldlr, Slc40a1*). Similarly, gene expression in the em-MG clusters of CD11b+ brain cell transplant group were highly correlated with the em-MG clusters in endogenous, untransplanted control (**Figure S3G, Supplementary Table 2**).

Untransplanted, PLX-treated mice were nearly devoid of sequenced microglia, except for a persistent population in the DAM cluster, consistent with prior studies reporting the relative resistance of amyloid plaque-associated microglia to depletion by CSF1R inhibition (**Figure S3D**) [12]. Interestingly, by pseudobulk comparison, these "PLX persistent" DAMs had only 4 differentially expressed genes compared to DAMs from untreated 5xFAD hosts (**Figure S3H, Supplementary Table 2**), reinforcing that the DAM gene program may not require normal CSF1R signaling. Altogether, these observations 1) validate prior studies showing clear differences between mo- and em-MGs following microglia replacement [36, 43] 2) extend this principle to DAMs, a disease-induced reactive state and 3) refine our understanding of the contribution of CSF1R signaling to the DAM program.

mo-MGs have intrinsically reduced DAM state plasticity

Our transplantation approach offers a unique opportunity to understand how macrophage ontogeny impacts the dynamic response of microglia to AD-like amyloid accumulation, in particular the transition from homeostatic to DAM state.

To address this question, we first compared baseline differences between em- and mo-MGs in homeostatic clusters. Top DEGs between em- and mo-MGs in WT hosts overlapped with those from prior studies that used a range of engraftment models (Fig. 4D). Notable themes included elevated mo-MG genes related to innate immune responses (e.g., *Cybb* and *Klra2*) [44, 45] and AD risk (e.g., *Ms4a* family members) [46]. Given growing awareness that lipid metabolism contributes to microglia dysfunction and AD, and the high expression of *Apoe* by mo-MGs [47, 48], we were struck to also see higher expression of multiple *Apoc* isoforms by mo-MGs. To more systematically evaluate lipid metabolism signatures, we scored homeostatic cluster MGs for expression of a curated microglia lipid gene set encompassing intake, transport, storage, and efflux genes based on key studies (*Apoe*, *Lpl*, *Apoc1*, *Fabp5*, *Abca1*, *Abcg1*, *Soat1*, *Plin2*, *Gpnmb*) [20, 47, 49, 50], as well as for gene ontology (GO)-defined cholesterol transport and metabolic processes. All were elevated in mo-MGs, regardless of host animal genotype or donor cell source (Fig. 4E-E**', S4A-A'**). Gene set enrichment analyses (GSEAs) corroborated the enrichment of immune response signatures in mo-MGs relative to transplanted and endogenous em-MGs, while showing a general enrichment effect of transplant itself on broader metabolism gene sets when comparing transplanted to endogenous MGs (Fig. 4F). Consistent with DEG analyses (**Figure S3G**), transplanted em-MGs had fewer enriched gene sets than mo-MGs, particularly in immune-related pathways. These analyses demonstrate that in murine microglia replacement, the transcriptional regulation of lipid metabolism and innate immune reactivity is shaped by macrophage ontogeny at baseline, with mo-MGs elevated for both programs even at homeostasis.

Adoption of the DAM signature represents a tightly regulated response to the amyloid plaque environment. An intriguing prior finding, aligned with our observations of altered lipid and immune gene regulation, is that mo-MGs show elevated DAM gene expression even with normal amyloid levels in a healthy WT host devoid of amyloid plaques [35, 41–42]. By including transplanted mo- and em-MGs in both WT and 5xFAD hosts, our study allows direct comparison of how these cell types transition from homeostatic to amyloid reactive states. Given the importance of lipid metabolism to DAM responses and amyloid pathology, we first compared lipid gene module scores between homeostatic and DAM microglia. While em-DAMs highly upregulated lipid metabolism networks compared to homeostatic em-MGs, mo-DAMs showed unchanged expression from mo-MGs (**Figure S4B-B'**).

To parse more specific differences in DAM state regulation, we individually examined stage 1 and 2 DAM cassettes as originally defined in Keren-Shaul et al., 2017 [20], the latter being Trem2 dependent. Em- and mo-DAMs similarly downregulated homeostatic/surveillance stage I DAM genes compared to their homeostatic counterparts (Fig. 5A-A'). However, they had very divergent patterns for the remaining stage 1 signature, which consisted of Apoe, immune activation and lysosomal priming genes. While stage I upregulated genes are highly induced by em-DAMs, they were already high in homeostatic mo-MGs, and thus only moderately increased in mo-DAMs. As expected, em-MGs induced the stage 2 cassette, which

consisted of genes involved in lipid metabolism, lysosomal degradation, phagocytosis, however in contrast, mo-MGs failed to strongly induce a stage 2 signature in mo-DAMs. These observations were consistent across donor cell types, including em- and mo-DAMs engrafted within the same brain in the CD11b+ brain cell transplant condition. Gene level comparison of the DAM signature further clarified that mo-DAMs retained high expression of *Apoe, Fth1*, and *Lyz2*, but not *Tyrobp, B2m, Ctsb*, and *Ctsd* from the Stage 1 cassette, and they fail to induce nearly all genes in the stage 2 cassette, including *Cst7, Ctsl, Cd9, Clec7a, Itgax, Csf1*, and *Ccl6*. (Fig. 5B, S5A-B). Finally, a recent study identified a DAM-like population of infiltrating macrophages, termed DIMs [51]. mo-DAMs share DIM ontogeny, and indeed, the mo-DAMs showed a larger increase in DIM module scores compared to em-DAMs (Fig. 5C).

In summary, homeostatic mo-MGs resemble stage I em-DAMs despite the absence of plaques. With pathologic brain amyloid accumulation, mo-MGs only slightly induce the overall DAM signature, fail to effectively engage the stage 2 cassette, and more broadly, to dynamically regulate lipid metabolic cassettes. Taken together, these transcriptomic analyses of microglia replacement in the 5xFAD model reveal a fundamental difference in how em- and mo-MG donor cells respond to amyloid.

Astrocyte gene expression is stable across microglia depletion and replacement

To more precisely explore how PLX treatment and microglia replacement impact astrocytes, we subclustered 41,839 cells expressing classical astrocytic marker genes (*Aqp4, Slc1a2, Slc1a3, Gja1*) after manual removal of minor contaminant clusters. Given the smaller size of our dataset compared to those powered to detect small subpopulations [52], we chose to avoid overparsing, merging transcriptionally similar subclusters into four distinct populations (Fig. 6A, S6A; **Methods**). Cluster identities were assigned by cross-referencing FindAllMarkers output against published mouse cortical astrocyte atlases (Fig. 6B): cluster 0 enriched for Chrdl1, consistent with homeostatic cortical gray matter astrocytes [52]; cluster 1 enriched for deep and outer layer gene *Agt* and glutamate receptor subunit *Gria1* [52–53]; cluster 2 enriched for lateral ventricular, subventricular, and deep cortical genes *Crym* and *Dkk3* [52, 54–55]; cluster 3, the smallest population identified, enriched for canonical interferon-stimulated genes *Ifit1, Ifit3*, and *Ifit3b* and master transcription factor *Stat1*, consistent with IFN responsive astrocytes [52]. Cluster 3 was omitted from downstream analyses due to insufficient cell numbers for meaningful comparison; consistent with an interferon-responsive identity, it was predominantly found in the 5xFAD condition (**Figure S6B**).

To understand how host genotype, PLX, and donor cell type impacted astrocytes, we first asked whether any of these variables impacted cluster distribution between conditions. Using propeller-based compositional analysis to test differences in cell proportions, we saw no significant difference across pairwise condition comparison after FDR correction (**Figure S6B**) [56].

Focusing next on gene expression, transcriptional state for each cluster was likewise stable across conditions, by three measures: (1) pseudobulk PCA segregated samples by cluster identity rather than by

host genotype, PLX treatment, or donor cell type, with all ten conditions distributed homogeneously within each cluster (Fig. 6C); (2) pairwise DGE on pseudobulk profiles identified only a handful of significant DEGs across conditions in both genotypes (**Figure S6C**); (3) module scoring across five canonical functional categories–including synaptic assembly, calcium-mediated signaling, cholesterol metabolic process, astrocyte activation, and blood brain barrier maintenance were unchanged across conditions (Fig. 6D, S6D). Together, these results show that, to the level of sensitivity of our data, astrocyte subcluster composition, transcriptional profile, and core functional programs were stable across microglia depletion and replacement in WT and 5xFAD hosts at early stages of plaque accumulation.

Oligodendrocyte gene expression is stable upon microglial depletion and replacement

Lastly, we subclustered 21,340 cells expressing canonical oligodendrocyte lineage marker genes (*Cldn11, Mog, Plp1, Mbp*), removing a small cluster with insufficient cells for analysis along with clusters identified as OPCs and likely neuronal contaminants. We resolved two clusters, again taking care to avoid overparsing, especially because we noted a less clear distinction between clusters in the top DEG heatmap (Fig. 6E, S6E; **Methods**), likely due to the continuum nature of oligodendrocyte gene expression. Cluster identities were assigned by cross-referencing FindAllMarkers output against published mouse brain oligodendrocyte atlases [57–58]. Though all clusters were overall very similar, cluster 1 enriched for *Enpp6*, a marker of newly formed oligodendrocytes while cluster 0 lacked distinct enriching markers (**Figure S6F**).

Like with astrocytes, propeller-based compositional analysis revealed no significant differences in subcluster proportions across any pairwise comparison (**Figure S6G**). Transcriptional state was likewise stable by the three measures applied to astrocytes, this time using oligodendrocyte gene modules (Fig. 6F-G, S6H). These results show that oligodendrocyte subcluster distribution, transcriptional profile, and core functional programs remained stable across microglia depletion and replacement in WT and 5xFAD hosts, to the level of sensitivity of our dataset.

DISCUSSION

The precise contributions of microglia to AD remain unresolved, in part because they are extraordinarily plastic and remodel their state within spatially confined tissue domains. Adding complexity, the brain parenchymal macrophage pool in human AD is likely a mix of primitive macrophages and infiltrating monocyte-derived cells whose contributions may differ or even oppose one another [22–23, 59–60]. To ask how donor cell source shapes the macrophage response to pathology, and its consequences, we developed an immunocompetent microglia replacement platform in which endogenous microglia are depleted and replaced by stereotaxic injection of inhibitor-resistant donor macrophages within the same amyloid-laden brain environment. In addition to providing new research tools, our study yields two

primary insights about how the brain environment and macrophage ontogeny interact in health and disease.

First, transplanted microglial surrogates from different sources have large transcriptomic differences both at baseline and in response to amyloid aggregation, dependent on a cell's original ontogeny, and preserved even after weeks-long in vitro expansion or conditional immortalization. While em-MGs efficiently induce DAM signatures in response to amyloid, mo-MGs have a stage 1 DAM-like state at baseline, and fail to effectively induce the stage 2 DAM cassette. This blunted response may either cause, or follow from, the reduced plaque interactions observed in mo- compared to em-MGs [61–62].

Second, however, these large transcriptional differences between donor populations were not accompanied by commensurate changes in the rest of the brain. Donor cell type, prolonged microglia absence, and sustained CSF1R inhibition minimally changed amyloid burden, astrogliosis, and macroglial state, with only small differences in plaque area after CD11b+ brain cell transplant and in GFAP area after Hoxb8 transplant. Astrocyte and oligodendrocyte subcluster composition, pseudobulk profile, and core gene modules were stable across all conditions in both WT and 5xFAD hosts, despite continued PLX3397 treatment, and long term residence of transcriptionally distinct macrophage populations. A dissociation between microglial transcriptome and environmental impact aligns with prior work noting transcriptional differences between murine mo- and em-MGs without clear functional consequence [33, 41, 63]. Overall, our data show, to our knowledge for the first time, that macrophage ontogeny shapes not only baseline cell state but the subsequent transcriptional response to amyloid pathology, without proportional effect on the surrounding tissue. As detailed in the limitations section, these conclusions are bounded by our study design, that applies an aggressive murine amyloid model, harvested between 4.5 and 5 months, assayed by neuropathology and single cell RNAseq.

That sustained CSF1R inhibition did not alter 6E10 immunoreactive area contrasts with important prior reports [12, 64], however mixed results across other studies [12, 65–66] suggest a high sensitivity to model and treatment paradigm used, including PLX dose, duration, and timing. Differences in pathology severity between animal colonies, related to microbiome or genetic background, may also contribute [67–68]. Lastly, we focused quantification on the dorsal subiculum, where plaques persist in association with spared, inhibitor-resistant microglia in multiple of these studies.

New tools to study the interactions between ontogeny, microglial identity, and neurodegenerative disease progression have become especially important in light of several recent discoveries. Lineage tracing in human brain, through analysis of somatic mutations, shows that monocyte-derived cells commonly enter the parenchyma and give rise to cells transcriptionally indistinguishable from resident microglia, but that strongly modify disease through unresolved mechanisms [22–23, 59–60]. In contrast, two recent xenotransplant studies, comparing brain-engrafted iPSC-derived microglia with peripheral blood monocytes, report transcriptional differences that resemble those we here describe, but the presence of mo-MGs is associated with inflammation, synapse and neuron loss, and altered behavior [69–70]. Whether that outcome follows from ontogeny itself, or from the xenotransplant setting, and whether

naturally infiltrating monocytes have similar effects, remains unresolved, but another key study demonstrates that as in human, spontaneously engrafting monocytes converge on the endogenous microglial program [71]. The contrasting results between spontaneous and evoked microglia replacement suggest that they may be fundamentally different processes; our platform isolates evoked replacement in an immunocompetent host, turning ontogeny into an experimental variable rather than a confound. It will be particularly exciting to use CRISPR-based screening approaches to elucidate the genetic underpinnings of differences between mo- and em-MGs, and their impacts on AD progression.

These topics are important for both existing and future therapies. Microglia replacement through HSCT is already a treatment and a gold standard for some leukodystrophies and lysosomal storage diseases. This precedent makes it clear that healthy donor cells can serve as powerful disease modifying agents in humans, regardless of origin. But whether donor cells, regardless of origin, converge on a microglial program like naturally infiltrating monocytes do, or retain a mo-MG signature - and whether this matters functionally, is now a pressing uncertainty. Our results raise that ontogeny need not be viewed as a fixed property, but one specifiable through donor cell selection and engineering, alongside the transgenes, enzymes, and receptors that replacement therapies can deliver.

LIMITATIONS

First, transcriptomic signatures belie microglia state but do not prove function. Second, in our model, microglia replacement or sustained CSF1R inhibition did not alter amyloid burden, astrogliosis, or macroglial state. These negative results cannot rule out an impact of microglia replacement on other models, timepoints, or phenotypes not tested or below our threshold of detection. Overall, plaque burden in our cohort appeared lower than published reports for 5xFAD, which may reduce sensitivity to detect differences in amyloid [12, 64]. Third, while our sequencing dataset is substantial (31 mice, 150,899 cells, 3–4 true biological replicates per group) and is well powered for the large ontogeny-driven differences we report, it is underpowered for sparse populations, including interferon-responsive microglia and astrocytes, about which we therefore refrained from drawing strong conclusions. We did not deeply analyze neurons, OPCs, vascular or stromal cells, data we provide for other investigators. Finally, transplanted cells were studied in animals receiving continuous CSF1R inhibitor and stereotaxic injection and expressing CSF1R^{G793A}, whereas endogenous microglia were profiled in untreated controls. These variables, however, would be expected to exaggerate differences between transplanted cells and endogenous microglia, which strengthens our finding that transplanted em-MGs closely resemble endogenous microglia.

MATERIALS AND METHODS

Mice

All animal studies were performed with approval from the Children's Hospital of Pennsylvania and the University of Pennsylvania Institutional Animal Care and Use Committees (IACUCs) in accordance with

institutional and national regulations. Animals were housed in a non-barrier facility with 12-h light/dark cycles at 23 ± 2°C in ventilated cages, with no more than 5 animals per cage. Animals were provided standard chow and water ad libitum.

5xFAD+/- males (B6.Cg-Tg(APPSwFlLon,PSEN1*M146L*L286V)6799Vas/Mmjax; JAX:034848, MMRRC) were crossed with WT C57BL/6J females (JAX:000664) in house to generate WT or 5xFAD+/- males that were used as host. CSF1RG793A/G793A mice a28-29] were crossed to C57BL/6J-Ptprcem6Lutzy/J or CD45.1 mice (JAX:033076) to generate CSF1RG793A/+; CD45.1+/- mice. CSF1RG793A/+; CD45.1+/- mice were subsequently intercrossed to produce CSF1RG793A/G793A; CD45.1+/- and CSF1RG793A/G793A; CD45.1+/+ mice that were used to make donor cells.

PLX3397 treatment

To deplete endogenous microglia, 7 weeks old animals were fed PLX3397 diet 1 week prior to transplant and were kept on PLX3397 diet until harvest timepoint (for a total of 10–11 weeks period). PLX3397 chow was created by incorporating PLX3397 powder (Selleckchem, S7818) into AIN-76A standard chow at 600 mg/kg dose (Research Diets).

exHSPC isolation and ex vivo expansion

exHSPC were isolated and cultured as described in Wilkinson et al., 2019 and Wilkinson et al., 2020 [30–31], with the modification of 5% oxygen to support HSPC expansion. Whole bone marrow was isolated from tibia, femur, and pelvis of 6–12 weeks old CSF1RG793A/G793A; CD45.1+/+ male mice, upon flushing of bones crushed with mortar and pestle (Fisher Scientific, S89638) with 1x PBS. Following a 100 μm filtering step, bone marrow cells were enriched for c-Kit+ cells using MACS CD117 microbeads (Miltenyi Biotec, 130-091-224) according to manufacturer's instructions. cKit enriched cells were subsequently grown in HSC media (F12 medium (Fisher Scientific, 11765062), 1x insulin-transferrin-selenium-ethanolamine (Thermo Fisher, 51500056), 10 mM HEPES (Invitrogen, 15630080), 1x penicillin-streptomycin-glutamine (Thermo Fisher, 10378016), and 1 mg/mL polyvinyl alcohol (PVA; Sigma, P8136-250G)) supplemented with 100 ng/mL murine thrombopoietin (TPO; Thermo Fisher, 315-14-100 UG) and 10 ng/mL murine stem cell factor (SCF; Thermo Fisher, AF-250-03-10 UG) in a 24-well CellBIND plate (Millipore, CLS3337-50 EA) at 0.5-1M cells/mL in each well at 37˚C with 5% CO2 and 5% O2. Cells were grown and expanded for 2 weeks post-harvest, during which media was replaced every 2–3 days and after which cells were split to maintain at a density of 0.5-1M cells/mL for each well. HSPC culture purity was evaluated via the KSL flow cytometry panel 2 weeks post-harvest. All transplants used exHSPCs with > 70% KSL+ fraction.

Bone marrow harvest

Bone marrow was harvested as described in Bennett et al., 2016 [72]. Femurs and tibias were collected from a 6 weeks old CSF1RG793A/G793A; CD45.1+/- male mouse. Whole bone marrow was flushed out of the bones with cold 1x PBS (Invitrogen 10010023) using a 1 mL syringe and treated with ACK lysis buffer (Quality Biological, 118-156-101) for 5 minutes at room temperature (RT) to lyse red blood cells.

Following a 1x PBS wash, cells were pelleted at 200 x g for 5 min at 4˚C in RPMI (Invitrogen, 7240047) for Hoxb8 progenitor immortalization.

Hoxb8 progenitor immortalization

Myeloid progenitors were immortalized as described in Wang et al., 2006 [32]. For Hoxb8 donor cell transplant, myeloid progenitors were isolated from whole bone marrow via density gradient centrifugation using Percoll (Cytiva, 17544501). Whole bone marrow was resuspended in R10 media (10% fetal bovine serum (VWR, 89510-186), 1% penicillin/streptomycin (Invitrogen, 15140122), and 1 mM sodium pyruvate (Invitrogen 11360070) in RPMI), followed by Percoll density centrifugation–where 4 mL density Percoll (45% Percoll in RPMI) were slowly layered beneath cell suspension and centrifuged at 600 x g for 20 minutes at room temperature with no brake. Isolated progenitors were grown in R10 media supplemented with 10 ng/mL IL-3 (Peprotech, 213 – 13), IL-6 (Peprotech, 216 – 16), and SCF (Peprotech, 250-03) for 3 days. Cells were infected with MSCVneo-HA-ER-Hoxb8 virus via centrifugation (1000 x g for 90 min at 22˚C) and were subsequently grown in R10 media supplemented with 0.5 μM beta-estradiol (Sigma Aldrich, E2758) and 10 ng/mL GM-CSF (Peprotech, 315-03). Transduced cells were recovered 24 hours post transduction, grown for 2 days, and selected against non-immortalized cells with 1 mg/mL geneticin for 48 hours (Thermo Fisher, 10131035). Antibiotic treated cells were fed with fresh cytokine supplemented media, expanded and passaged every 2–3 days at 25-50K cells/mL for 2–3 weeks, or until non-immortalized cells were terminally differentiated or were killed.

Virus production

Virus was produced as described in Nemec et al., 2025 [33]. Hoxb8 virus was generated by transfecting Lenti-X 293 T cells (Takara Bio, 632180) with 850 ng/mL pCL-Eco retrovirus packaging plasmid (Addgene, 12371) and 850 ng/mL MSCVneo-HA-ER-Hoxb8 transfer plasmid (Igor Brodsky, University of Pennsylvania School of Veterinary Medicine) using 5 μL LipoD293 (SignaGen, 504782) in DMEM media (Thermo Fisher, 10569010). Transfection media was replaced with fresh D10 media (DMEM, 25 mM HEPES, 10% FBS, and 1% Penn/Strep) 6 hours post-transfection. Viral supernatants were collected 48 and 72 hours later and concentrated in Retrovirus Precipitation Solution (Alstem, VC200) according to manufacturer's instructions.

Microglia isolation

Single cell isolation of microglia and macrophage from the mouse brain for flow cytometry analyses was performed as described in Bennett et al., 2016 [72]. Donor microglia were isolated from P4-P7 CSF1RG793A/G793A; CD45.1+/+ male and female mice. Adult microglia and macrophage were isolated from 4.5-5 months old WT and 5xFAD+/- mice. Neonatal mice were cryoanesthetized on ice for 5–8 minutes and adult mice were anesthetized using a 100 mg/kg ketamine and 10 mg/kg xylazine cocktail made up in 1x PBS. Upon achieving anesthetic depth as indicated by lack of pedal reflex, mice were transcardially perfused in 15 mL (neonate) or 20 mL (adult) cold PBS. All subsequent steps were performed on ice or in centrifuge that was prechilled to 4˚C. All buffers, reagents, conical tubes, and dounce homogenizers were prechilled. Brains were collected and dounce homogenized in 7 mL of cold

medium A buffer (15 mM HEPES and 0.5% glucose (Sigma, G7021-1KG) in 1x Hank's balanced salt solution (Thermo Fisher, 14185052)) for a total of 3–4 plunges. Homogenized tissue was filtered through a 70 µm strainer (Fisher Scientific, 08-77-2) and pelleted at 200 x g for 7 minutes. Myelin debris was separated and removed from the cell suspension following isotonic Percoll centrifugation (30% Percoll in HBSS at 700 x g for 20 minutes). Following two cold medium A washes, cells were either enriched using MACS CD11b microglia isolation kit (Miltenyi, 130-093-636) according to manufacturer's instructions and were resuspended at 250K/µL 1x PBS for donor cell transplant or were resuspended in 1x PBS for flow cytometry staining and analysis.

Stereotaxic injection in adult mice

Stereotaxic injection was performed as described in Lombroso et al., 2026 [29]. Experimental mice were placed on 600 mg/kg PLX3397 diet 7 days before transplant. For donor cell transplant, 2 months old PLX3397 treated mice were anesthetized in an isoflurane chamber and positioned on a stereotaxic rig (Kopf, Model 940). Upon achieving anesthetic depth as indicated by lack of pedal reflex, mice were given a dose of analgesic (5 mg/kg meloxicam delivered subcutaneously) and ophthalmic ointment (Dechra, 17033-211-38) was applied. The skull was then secured by inserting non-rupture ear bars (Kopf, Model 922) into the external auditory meatus. Incision site was cured 3 times with alternating 10% povidone-iodine (RICCA, R3955000-500B) and 1x PBS, after which an incision was made to perforate the subcutaneous and muscle tissue above the skull. Bregma became the designated zero point (anterior-posterior, medial-lateral, dorsal-ventral coordinate of 0, 0, 0 mm) for identifying target coordinate for the hippocampus (-2.3, +/-1.75, -1.8 mm). Once located, a 1–2 mm burr hole was made at target injection site using a hand drill. A sterilized NanoFil syringe needle (World Precision Instruments, NANOFIL; NF33BV) pre-loaded with 1 µL of donor cells was lowered into the hippocampus for donor cell delivery at a constant flow rate of 300 nL/min. Upon injection, needle was incubated for 2 minutes before being slowly raised to the surface. Skin was sealed using Vetbond Tissue Adhesive (Midwest Veterinary Supply, 470.00369.4). Animals were monitored for a total of 3 days post-surgery, with a second postoperative dose of 5 mg/kg meloxicam being delivered day after surgery.

Immunofluorescence staining

Mice were anesthetized using a 100 mg/kg ketamine and 10 mg/kg xylazine cocktail in 1x PBS and were transcardially perfused with 20 mL 1x PBS, followed by 20 mL of 4% paraformaldehyde (PFA; w/v in 1x PBS; Electron Microscopy Sciences, 19200). Brains were dissected, drop-fixed in 4% PFA for 22–24 hours at 4˚C, incubated in 30% sucrose (Sigma Aldrich, S1888-5KG) for 48 hours at 4˚C, and embedded in O.C.T. compound (Fisher Scientific, 23-730-571) on dry ice. Frozen tissues blocks were cryosectioned at 16 µm and mounted onto Superfrost Plus slide (Fisher Scientific, 1255015). Tissues were dehydrated on the slide warmer at 60˚C for 5–10 minutes and slides were stored at -80˚C until use.

For immunofluorescence staining, frozen slides were warmed on the slide warmer at 60˚C for 5 minutes, rehydrated in 1x PBS at RT for 5 minutes, blocked with blocking buffer at RT for 1 hour, stained with primary antibodies at RT for 1 hour, washed 3 times in 1x PBS for 5 minutes each, stained with

secondary antibodies at RT for 1 hour, washed 3 times in 1x PBS for 5 minutes each, mounted in DAPI mounting media (Electron Microscopy Sciences, 17989-60), coverslipped (Sigma Aldrich, 48393-106), and sealed with clear nail polish. Blocking buffer was prepared fresh as follows: 10% donkey serum (Sigma, S39-100ML), 0.5% Triton X-100 (Sigma, T8787-50ML), in 1x PBS. Antibody staining buffer was prepared fresh as follows: 1% donkey serum, 0.5% Triton X-100 in 1x PBS. Primary antibodies used include rabbit anti-IBA1 (1:250; Wako, 019-19741), rabbit anti-GFAP (1:1000; Dako, Z0334), rat anti-CD68 (1:500; Biolegend, 137001), and mouse anti-6E10 (1:1000; Biolegend, 803001). Secondary antibodies used include donkey anti-rat Alexa Fluor 488 (Invitrogen, A21208), donkey anti-mouse Alexa Fluor Plus 555 (Invitrogen, A32773), donkey anti-rabbit Alexa Fluor Plus 555 (Invitrogen, A32794), donkey anti-mouse Alexa Fluor 647 (Invitrogen, A32787), and donkey anti-rabbit Alexa Fluor Plus 647 (Invitrogen, A32795).

Image acquisition, processing, and analysis

Stained tissue sections were imaged using Keyence BZ-X800 fluorescence microscope with 10x and 20x objectives. While the 10x objective was used to collect images for qualitative and quantitative analysis for IBA1 and CD68 (Fig. 1, 2B), the 20x objective was used for 6E10 and GFAP (Fig. 2A, 2C). Same exposure settings were applied to samples within an experiment during image acquisition. For 10x tile images, individual images were stitched together using Keyence Analyzer software prior exporting in the .tif format.

For CD68, GFAP, and 6E10 percent area analyses, signal was detected by applying an intensity threshold onto the image to create a binary mask in FIJI (ImageJ). Area measured by the mask was divided by total tissue area, and multiplied by 100% to calculate percent area. For Iba1 percent area and cell count, signal was detected using surface machine learning segmentation in Imaris v10.2 (Oxford Instruments) to delineate nucleated, IBA1 expressing cells with a cell body and 1 or more processes. For brain engraftment analysis, coronal tissue area occupied by IBA1 expressing cells and whole coronal tissue area were traced using the polygon tool in FIJI. Percent area occupied was then calculated by taking the ratio of area occupied by IBA1 expressing cells across the coronal tissue and total coronal tissue area multiplied by 100%. For dot rendering of IBA1 expressing cells, IBA1 signal was converted into mask as reported by Chadarevian et al., 2023 [26], following background subtraction (rolling = 15), threshold adjustments (Otsu dark), and analyze particle tool (size = 40-1000 px, circularity = 0–1) in FIJI.

Flow cytometry

Staining was performed on ice or in a centrifuge prechilled to 4˚C. For chimerism analysis, cell suspensions were incubated with 0.2% CD16/CD32 (BD Biosciences, 553142) in 1x PBS for 10 minutes to block Fc receptors and with LIVE/DEAD fixable aqua dead cell stain kit (1:200 in 1x PBS; Thermo Fisher, L34965A) for 5 minutes to identify live cells. Following Fc block, cells were immunostained with fluorophore-conjugated antibody cocktail for 30 minutes, washed twice with FACS buffer (0.5% BSA (Sigma Aldrich, 126609-10GM), 0.5 mM EDTA (Thermo Fisher, 15575020) in 1x PBS), and resuspended with propidium iodide (PI; 1:1000 in FACS buffer; Invitrogen BMS500PI) containing FACS buffer before

being analyzed on the CytoFLEX LX (6 lasers, 21 detectors). Antibodies used for the chimerism panel include anti-mouse CD11b-APC-Cy7 (clone M1/70; 1:200 in 1x PBS; Biolegend 101226), anti-mouse CD45.1-PE-Cy7 (clone A20; 1:50 in 1x PBS; Biolegend 110730), anti-mouse CD45.2-BV421 (clone 104; 1:200 in 1x PBS; Biolegend 109832), and anti-mouse TMEM119-PE (clone V3RT1GOsz; 1:100 in 1x PBS; Thermo Fisher, 12-6119-82). The gating strategy used is as follows: FSC-A vs SSC-A > FSC-A vs FSC-H > live/dead vs PI > CD11b vs SSC-A > CD45.1 vs CD45.2 > TMEM119 vs SSC-A. Flow data were collected on 6 separate experiments and gates were defined across experiments using $CD45.1^{+/+}$ and $CD45.2^{+/+}$ positive control samples for each experiment.

For KSL analysis, single cell suspensions were blocked with Fc block for 10 minutes, incubated with biotin-conjugated lineage antibody cocktail for 30 minutes, washed with 1x PBS, and pelleted at 440 x g for 5 minutes. Cell pellets were stained with fluorophore-conjugated HSC antibody cocktail for 30 minutes, washed twice with 1x PBS, resuspended in PI containing FACS buffer, and analyzed on the flow analyzer. Biotin-conjugated lineage antibodies include anti-Ly-6G/Ly-6C (clone RB6-8C5; 0.15 mg/mL in 1x PBS; Thermo Fisher, 13-5931-82), anti-Ter119 (clone Ter119; 0.15 mg/mL in 1x PBS; Thermo Fisher, 13-5921-82), anti-CD4 (clone RM4-5; 0.035 mg/mL in 1x PBS; Thermo Fisher, 13-0042-85), anti-CD8a (clone 53 – 6.7; 0.035 mg/mL in 1x PBS; Thermo Fisher, 13-0081-85), anti-CD45R (clone RA3-6B2; 0.75 mg/mL in 1x PBS; Thermo Fisher, 13-0452-82), and anti-CD127 (clone A7R34; 0.75 mg/mL in 1x PBS; Thermo Fisher, 13-1271-82). HSC antibodies include rat anti-mouse c-Kit-APC (clone 2B8; 0.5 µg/mL in 1x PBS; Thermo Fisher, 17117182), rat anti-mouse Sca1-PE (clone D7; 0.5 µg/mL in 1x PBS; Biolegend, 108108), Streptavidin-APC-eFluor780 (0.5 µg/mL in 1x PBS; Thermo Fisher, 47431782), and rat anti-mouse CD150-PE-Cy7 (clone TC15-12F12.2; 0.5 µg/mL in 1x PBS; Biolegend, 115914). The gating strategy used is as follows: FSC-A vs SSC-A > FSC-A vs FSC-H > FSC-A vs PI > FSC-A vs Streptavidin > Sca-1 vs c-Kit > FSC-A vs CD150.

Flow cytometry data were analyzed in FlowJo V10 (BD Biosciences).

Single cell isolation

Working buffer and solution for single cell isolation were made fresh and filter sterilized on harvest day. Except for digestion buffer which was kept at 34˚C, all buffers, solutions, and protein LoBind tubes were prechilled on ice or are kept at 4˚C. Perfusion, dissection, and digestion buffers, as well as transcriptional and translational inhibitor stocks were prepared as described in Marsh et al., 2022 [39]. For perfusion buffer, transcriptional inhibitors actinomycin (5 µg/mL; Sigma Aldrich, A1410-5MG) and triptolide (10 µM; Sigma Aldrich, T3652-1MG) were added to 1x HBSS w/o Ca2+, Mg2+ (ThermoFisher, 14175095) to inhibit *ex vivo* activation of microglia. For dissection buffer, actinomycin, triptolide, and translational inhibitor anisomycin (27.1 µg/mL; Sigma Aldrich, A9789-5MG) were added to 1x HBSS w/o Ca2+, Mg2+. For digestion buffer, papain (200 U/mouse; Worthington Biochemical, LS003126) was activated by L-cysteine (5.5 mM; Fisher Scientific, AAA1038914) in enzyme stock solution (0.5 mM EDTA and 0.46% glucose in 1x HBSS w/ Ca2+, Mg2+ (Mediatech, MT21-023-CV)) and used within 30 minutes of activation. All 3 inhibitors were then added to the digestion buffer immediately before use, followed by DNase I (2500 U/mouse; Worthington Biochemical, LS002007) to degrade exogenous DNA from dead

cells and prevent cell clumping. Ovomucoid (Worthington Biochemical, LS003087), used to quench enzymatic activity of papain, was prepared as described in Foo, CSHP 2013; that is at low (1.5 mg/mL ovomucoid, 1.5 mg/mL BSA in 1x D-PBS w/ Ca2+, Mg2+ (Gibco, 14287080), with pH adjusted to 7.4) and high (3.0 mg/mL ovomucoid, 3.0 mg/mL BSA in 1x D-PBS w/ Ca2+, Mg2+, with pH adjusted to 7.4) concentrations, with DNase I added before use. 0.02% BSA suspension solution was prepared in 1x D-PBS w/ Ca2+, Mg2+, with DNase I added before use.

Harvested tissue and cell suspension were kept cold on ice or in centrifuge prechilled to 4˚C throughout the isolation, with the exception for digestion and dead cell removal steps that were performed at 34˚C or at RT, respectively. Mice were anesthetized using a 100 mg/kg ketamine and 10 mg/kg xylazine cocktail in 1x PBS and were transcardially perfused with 20 mL cold perfusion buffer. Dissected brains were kept on ice in dissection buffer until harvest had been completed, after which they were dissected for cortex and hippocampus, chopped into 1 mm3 pieces, and transferred into papain digestion buffer. Tissue fragments were incubated at 34˚C for 20 minutes and inverted 4–5 times every 5 minutes. Digested tissues were gently triturated in low ovomucoid until 90–95% tissue chunks remained. Trituration was completed through 6–7 rounds with 50 repetitions each round, allowing for tissue to settle in between rounds and working first from wide bore pipette to progressively narrow bore pipette (i.e. serological pipette > cut P1000 tip > uncut P1000 tip) across rounds. Supernatant was collected at the end of each round. Cell suspension was pelleted in high ovomucoid at 110 x g for 5 min, resuspended in 0.02% BSA, and filtered through 40 µm strainer (Bel-Art, 13680-0040). Myelin debris was removed using density gradient centrifugation the debris removal solution (Miltenyi Biotec, 130-109-398) according to manufacturer's instructions. Dead cells were removed using dead cell removal kit (Miltenyi Biotec, 130-090-101) according to manufacturer's instructions. Cells were manually counted and viability of > 70% was verified using a hemocytometer prior to being loaded onto a 10X Chromium chip.

Single cell partitioning, library generation, and sequencing

Single cell RNA-seq experiment was performed using 10x Genomics GEM-X Universal 3' Reagent Kits v4 4-plex. 5000 and 8300 cells/well were targeted and loaded, respectively, onto the Chromium GEM-X OCM chip according to the manufacturer's instructions. Chips were loaded into the Chromium X controller for GEM droplet generation and barcoding, following which cDNA synthesis, amplification, and library construction were performed according to manufacturer's instructions. GEX libraries were quality controlled using Agilent 2100 Bioanalyzer and the High Sensitivity DNA Analysis kit (Agilent, 5067 – 4626) and sequenced at sequencing depth of 30-50K reads/cell using Illumina NovaSeq 6000 V1.5 chemistry at the Children's Hospital of Philadelphia Center for Applied Genomics (CAG) sequencing core.

Single cell pre-processing and analysis

Raw sequencing reads were demultiplexed and aligned to the GRCm39 mouse reference genome customized to include human APP and PSEN1 transcripts using Cell Ranger (v9.0.1, 10x Genomics). Downstream analysis was performed in R (v4.3.3) using Seurat (v5.0.1). For quality control, low quality cells, empty droplets, and putative multiplets were filtered out by excluding cells with fewer than 1000 or

more than 25,000 UMIs, fewer than 500 or more than 6,000 detected genes, greater than 10% mitochondrial or 30% ribosomal reads, or low complexity (log10GenesPerUMI < 0.8). Raw counts were normalized in Seurat using the SCTransform method, which applies regularized negative binomial regression to account for technical variability. The S.score variable in SCTransform was derived from normalizing raw counts using the log-normalization method, which divided counts for each cell by total counts for the cell and multiplied by a scale factor of 10,000, and this output was then natural log-transformed. The top 3,000 highly variable features were identified using the variance stabilizing transformation method, which models the relationship between log(variance) and log(mean) using local polynomial regression to standardize feature values. Linear dimensionality reduction was then performed on these 3,000 highly variable genes using PCA. The top 15 principal components were used to generate the whole CNS UMAP for nonlinear dimensionality reduction. Cell populations were initially annotated using two complementary automated approaches: SingleR, with the Tabula Muris dataset [73] as the reference and pruning of low-confidence assignments, and scType, which assigns identities based on established cell-type-specific marker genes. Final annotations were determined by manual review of the combined SingleR and scType results together with canonical marker expression and known CNS biology, supported by reference databases including PanglaoDB [74] and CellMarker 2.0 [75].

CELL TYPE SPECIFIC RECLUSTERING

Microglia, astrocytes, and oligodendrocytes were extracted from the annotated whole CNS object for independent reclustering. For the microglia and macrophage subset, cells annotated as microglia and macrophage were retained (and analogously for the astrocyte and oligodendrocyte lineages). Within each subset, outlier cells were removed by median absolute deviation (MAD) filtering on the number of detected genes, UMI counts, and percent mitochondrial reads, using a threshold of 4 MADs from the median. Following quality control, raw counts were applied through the same analysis pipeline as the whole CNS dataset, starting from SCTransform.

For microglia/macrophage analyses, subclusters were excluded from downstream analyses if they exhibited uniformly low UMI distributions relative to retained subclusters, and did not resolve stably from clearly contaminating astrocyte clusters across the range of clustering resolutions tested (resolution 0.4–1.4). This affected 2 subclusters of 1615 and 1464 total cells. Cells within excluded subclusters met global per-cell QC thresholds; exclusion was applied at the subcluster level on the basis of aggregate transcriptional features and clustering stability rather than per-cell filtering. Excluded subclusters and their distribution are shown in **Figure S3A**. Clusters within the myeloid subset were annotated by curated cell identity and cell state marker genes.

Astrocytes were subclustered at resolution 0.4, yielding 10 clusters (**Figure S6A**). Clusters in both datasets were annotated from the top 20 DEGs per cluster (Seurat FindAllMarkers), and those without biologically meaningful differences were merged. Cluster 4 (408 cells) expressed canonical microglial genes (*C1qb, C1qc, Tyrobp, Ctss, Fcrls, Mrc1, Ly6e*) and was removed, resulting in 4 clusters for analysis. Oligodendrocytes were subclustered at resolution 0.2, yielding 5 clusters (**Figure S6E**). Cluster 4 (25

cells) was removed due to low cell number; cluster 3 (338 cells, *Bmp4/Vcan/Gpr17*) and cluster 2 (949 cells, *Man1a/Synpr/Cntn1/Pcsk7*) were identified as OPCs and likely neuronal contaminants, respectively, and removed. Marker gene heatmaps (Fig. 3C, 6B, S6F) were computed by Wilcoxon rank-sum test on a per-cell normalized expression, comparing each cluster against all others.

PROPORTION OF CELLS ANALYSIS

The proportion of cells in each cluster was computed per experimental condition to compare cluster composition across conditions. To identify statistically significant compositional shifts, propeller function from speckle R package (v1.12.0) [56] was applied in a one vs. rest design, comparing each condition against all remaining conditions combined.

PSEUDOBULK PCA

To provide an exploratory overview of transcriptional structure, single cell counts were aggregated into pseudobulk profiles by sample, experimental group, and cluster. Pseudobulk counts were variance stabilized with DESeq2 (vst, blind = TRUE) and the top 2,500 most variable genes were selected based on row-wise variance. The matrix was transposed and PCA was computed with prcomp (centering enabled, without unit-variance scaling). Mean values of each sample were plotted.

PSEUDOBULK DIFFERENTIAL EXPRESSION ANALYSIS

Prior to modeling, gene-level counts were aggregated at the sample and cluster level (pseudobulk) by summing cells within each sample and cluster for all comparisons, except for microglial WT vs 5xFAD comparison, where counts were aggregated by sample only. We followed the pseudobulk differential expression workflow of decoupleR [76], in which counts were aggregated per sample and cell population, low quality pseudobulk samples and lowly expressed genes were filtered, and each population was separately analyzed.

Pseudobulk samples comprising fewer than 10 cells were removed. Lowly expressed genes were filtered using the filterByExpr function from R package edgeR v3.42.4 (min.count = 10), with the condition supplied as the grouping variable such that the minimum group size used for filtering was determined from the smallest experimental group rather than from all samples pooled. Genes passing filterByExpr were additionally required to be detected in at least 10% of the cells in two or more samples. Counts were normalized using the TMM method (calcNormFactors) and transformed with voom to obtain log-CPM values and the associated precision weights. Normalized gene expression values were used to fit the linear regression model using lmFit (limma v3.56.2) [77]. Each contrast was resolved to the subclusters its conditions occupy, and contrasts sharing the same subcluster set were fitted together in a single model, from which all corresponding comparisons were extracted. For the microglia, homeostatic contrasts were fitted on the em-MG, mo-MG subclusters; DAM contrasts on em-DAM and mo-DAM; and homeostatic-vs-DAM contrasts on all four subclusters combined. Within each fit, condition was the model covariate. Empirical Bayes moderation was applied with robust variance estimation (eBayes, robust = TRUE) and p-values were corrected for multiple testing using the Benjamini-Hochberg

method. This pseudobulk differential expression pipeline was used to generate the DEG heatmap (Fig. 4D), volcano plots (**Figure S3F**), and scatter plots (Fig. 3G-H).

To distinguish genuine expression changes from differences driven by cell type composition, we compared the proportion of each microglial subtype between the two groups for every contrast and recorded the largest change in subtype proportion, using propeller (speckle package) [56] to evaluate statistical significance in proportion differences across biological replicates. Compositionally balanced contrasts include all Hoxb8 vs. exHSPC (0.2% shift for WT homeostatic population), PLX persistent vs. control (1.5% shift for 5x DAM population), and endogenous vs transplanted em-MG (1.1% for WT homeostatic population) contrasts; these contrasts were interpreted condition effects. Compositionally imbalanced contrasts include em-MG vs mo-MG contrast (97.6% shift in WT homeostatic population); this contrast was interpreted as reflecting differences between populations.

PATHWAY ANALYSIS

GSEA was performed on the pseudobulk differential expression results from pairwise comparison. Genes were ranked based on the sign of their log fold-change and the − log transformed p-value, placing the most significantly upregulated genes at the top of the ranked list and the most significantly downregulated at the bottom. Pathway enrichment analysis was computed with the GSEA software (gsea-msigdb.org) [78] against the hallmark gene set collection over gene sets containing 10–500 genes, using the classic unweighted scoring scheme, meandiv normalization, and 1,000 permutations.

For the proportion of clusters, DGE, and GSEA pathway analyses, P-values were adjusted for multiple testing by the Benjamini–Hochberg method, and clusters, gene expression, and pathways, respectively, with an adjusted p (q-value) < 0.05 were considered significantly different.

MODULE SCORING

Gene modules were defined by Gene Ontology (GO) terms or curated gene lists (**Supplementary Table 3**). Module scores were calculated for each cell using the Seurat function AddModuleScore, which computes the average expression of the genes in each module. Microglia identity module was constructed from gene sets derived from Bennett et al, 2018, Cronk et al., 2018, and Shemer et al., 2018; [35, 41–42]. HSC lineage module was composed of gene sets defined in Bennett et al, 2018, Shemer et al., 2018, and Pombo Antunes et al., 2021 [35, 42, 79]. Combined Stage 1 and 2 upregulated DAM, Stage 1 downregulated DAM, Stage 1 upregulated DAM, and Stage 2 upregulated DAM modules were defined in Keren-Shaul et al., 2017 [20]. DIM conserved gene module was as defined in Silvin et al., 2022 [51]. Lipid metabolism module was constructed from gene sets defined in Keren-Shaul et al., 2017, Krasemann et al., 2017, Nugent et al., 2020, and Marschallinger et al., 2020 [20, 49–50, 47]. Synaptic assembly module was constructed from genes identified by Christopherson et al., 2005, Allen et al., 2012, Kucukdereli et al., 2011, and Blanco-Suarez et al., 2018 [80–83]. GO-defined gene sets used in this study included cholesterol transport module (GO:0030301), cholesterol metabolic process module (GO:0008203), astrocyte activation module (GO:0048143), calcium-mediated signaling module (GO:0019722), blood brain barrier maintenance module (GO:0014032), myelination module

(GO:0042552), lipid biosynthetic process module (GO:0008610), neuron projection maintenance module (GO:1990535), axon ensheathment module (GO:0008366), unfolded protein response module (GO:0006986), and response to oxidative stress module (GO:0006979).

Abbreviations

5xFAD Five familial Alzheimer's disease mutations (transgenic model)

6E10 Anti-amyloid-β monoclonal antibody clone 6E10

AD Alzheimer's disease

BAM Border-associated macrophage

CD11b+ Br Primary CD11b+ cells isolated from early postnatal brain

CNS Central nervous system

CRISPR Clustered regularly interspaced short palindromic repeats

CSF1R Colony-stimulating factor 1 receptor

DAM Disease-associated microglia

DEG Differentially expressed gene

DGE Differential gene expression

DIM Disease inflammatory macrophage

em-MG Embryonic-origin microglia

exHSPC Ex vivo expanded hematopoietic stem and progenitor cells

FDR False discovery rate

GFAP Glial fibrillary acidic protein

GO Gene Ontology

GSEA Gene set enrichment analysis

Hoxb8 Homeobox B8 (conditionally immortalized myeloid progenitors)

HSC Hematopoietic stem cell

HSCT Hematopoietic stem cell transplantation

HSPC Hematopoietic stem and progenitor cell

IBA1 Ionized calcium-binding adapter molecule 1

IFN Interferon

iPSC Induced pluripotent stem cell

JAK/STAT Janus kinase/signal transducer and activator of transcription

MFI Median fluorescence intensity

MG Microglia

mo-MG Monocyte-derived microglia

OPC Oligodendrocyte precursor cell

PCA Principal component analysis

PLX / PLX3397 Pexidartinib, CSF1R inhibitor

QC Quality control

scRNA-seq Single-cell RNA sequencing

TMEM119 Transmembrane protein 119

UMAP Uniform manifold approximation and projection

UMI Unique molecular identifier

WT Wild type

Declarations

Ethics approval: All animal studies were performed with approval from the Children's Hospital of Pennsylvania and the University of Pennsylvania Institutional Animal Care and Use Committees (IACUCs) in accordance with institutional and national regulations.

Consent for publication: not applicable

Availability of data: Sequencing data are available in the GEO repository, accession GSE338311. To access data during peer review go to https://www.ncbi.nlm.nih.gov/geo/query/acc.cgi?acc=GSE338311, and enter token khetgeacxpgxpcd into the box. Additional information related to sequencing data is included within the supplementary file provided (**Supplementary Table 1**).

Competing interests: F.C.B. and M.L.B. are co-inventors on a patent filed by the board of trustees of the Leland Stanford Junior University (12612599), related to methods of microglia replacement. F.C.B. holds shares in Savanna Biotherapeutics, Inc. M.L.B. holds shares in Alector, Inc. L.V., D.K., M.M., and K.E. are employees of VUGENE.

Funding: F.C.B. is supported by NIH grant (R01NS129737-04) and Chan Zuckerberg Initiative grant (2023-331844). S.G. is supported by NIH grant (R01NS129737-04). M.B.L is supported by NIH grant (DP5OD036159). M.S.H. is supported by NIH grant (DP2AI192583). J.A. is supported by CHOP SPAR Fellowship. S.I.L is supported by NIH grant (GM008076), Blavatnik Family Fellowship, and NSF grant (NSF-GRFP DGE-1845298).

Authors' contributions: Conceptualization, CHO, SG, FCB.; Methodology, CHO, ELM, DAS, COB, JA, MRD, JA, SIL, SG, FCB; Software, VL, DK, MM; Validation, COH, ELM, COB, FY, MRD; Formal Analysis, CHO, ELM, DAS, COB, VL, DK, MM, MS; Investigation, CHO, ELM, COB, JA, FY, RNA; Resources, CHO, MSH, MLB, GS, FCB; Data Curation, CHO, VL, DK, MM, MS; Writing - original draft, CHO, SG, FCB.; Writing - reviewing and editing, CHO, ELM, DAS, COB, MRD, JA, FY, RNA, RJR, SIL, SG, FCB; Visualization, CHO, ELM, VL, DK, MM, FCB; Supervision, CHO, EK, SG, FCB; Project Administration, CHO, SG, FCB; Funding and Acquisition, SG, FCB.

Acknowledgements: We thank M. Zhang PhD, A. Yousey, X. Yang, K. Ostberg, Single Cell Technology Core at CHOP, and Center for Applied Genomics at CHOP for their valued contributions to this work. We thank Mathew Blurton-Jones, Hayk Davtyan, and Jean Paul Chadarevian for sharing the G793A mouse model.

References

1. Harold D, Abraham R, Hollingworth P, Sims R, Gerrish A, Hamshere ML, et al. Genome-wide association study identifies variants at CLU and PICALM associated with Alzheimer's disease. Nat Genet. 2009;41(10):1088–93. 10.1038/ng.440 . PubMed PMID: 19734902; PubMed Central PMCID: PMC2845877.
2. Naj AC, Jun G, Beecham GW, Wang LS, Vardarajan BN, Buros J, et al. Common variants at MS4A4/MS4A6E, CD2AP, CD33 and EPHA1 are associated with late-onset Alzheimer's disease. Nat Genet. 2011;43(5):436–41. 10.1038/ng.801 . PubMed PMID: 21460841; PubMed Central PMCID: PMC3090745.
3. Hollingworth P, Harold D, Sims R, Gerrish A, Lambert JC, Carrasquillo MM, et al. Common variants at ABCA7, MS4A6A/MS4A4E, EPHA1, CD33 and CD2AP are associated with Alzheimer's disease. Nat Genet. 2011;43(5):429–35. 10.1038/ng.803 . PubMed PMID: 21460840; PubMed Central PMCID: PMC3084173.
4. Lambert JC, Ibrahim-Verbaas CA, Harold D, Naj AC, Sims R, Bellenguez C, et al. Meta-analysis of 74,046 individuals identifies 11 new susceptibility loci for Alzheimer's disease. Nat Genet. 2013;45(12):1452–8. 10.1038/ng.2802 . PubMed PMID: 24162737; PubMed Central PMCID: PMC3896259.

5. Bertram L, Lange C, Mullin K, Parkinson M, Hsiao M, Hogan MF, et al. Genome-wide association analysis reveals putative Alzheimer's disease susceptibility loci in addition to APOE. Am J Hum Genet. 2008;83(5):623–32. 10.1016/j.ajhg.2008.10.008 . PubMed PMID: 18976728; PubMed Central PMCID: PMC2668052.
6. Guerreiro R, Wojtas A, Bras J, Carrasquillo M, Rogaeva E, Majounie E, et al. TREM2 variants in Alzheimer's disease. N Engl J Med. 2013;368(2):117–27. doi:10.1056/NEJMoa1211851 PubMed PMID: 23150934; PubMed Central PMCID: PMC3631573.
7. Jonsson T, Stefansson H, Steinberg S, Jonsdottir I, Jonsson PV, Snaedal J, et al. Variant of TREM2 associated with the risk of Alzheimer's disease. N Engl J Med. 2013;368(2):107–16. 10.1056/NEJMoa1211103 . PubMed PMID: 23150908; PubMed Central PMCID: PMC3677583.
8. Efthymiou AG, Goate AM. Late onset Alzheimer's disease genetics implicates microglial pathways in disease risk. Mol Neurodegener. 2017;12(1):43. 10.1186/s13024-017-. 0184-x PubMed PMID: 28549481; PubMed Central PMCID: PMC5446752.
9. Condello C, Yuan P, Schain A, Grutzendler J. Microglia constitute a barrier that prevents neurotoxic protofibrillar Aβ42 hotspots around plaques. Nat Commun. 2015;6:6176. 10.1038/ncomms7176 . PubMed PMID: 25630253; PubMed Central PMCID: PMC4311408.
10. Wang Y, Ulland TK, Ulrich JD, Song W, Tzaferis JA, Hole JT, et al. TREM2-mediated early microglial response limits diffusion and toxicity of amyloid plaques. J Exp Med. 2016;213(5):667–75. 10.1084/jem.20151948 . PubMed PMID: 27091843; PubMed Central PMCID: PMC4854736.
11. Yuan P, Condello C, Keene CD, Wang Y, Bird TD, Paul SM, et al. TREM2 Haplodeficiency in Mice and Humans Impairs the Microglia Barrier Function Leading to Decreased Amyloid Compaction and Severe Axonal Dystrophy. Neuron. 2016;90(4):724–39. 10.1016/j.neuron.2016.05.003 . PubMed PMID: 27196974; PubMed Central PMCID: PMC4898967.
12. Spangenberg E, Severson PL, Hohsfield LA, Crapser J, Zhang J, Burton EA, et al. Sustained microglial depletion with CSF1R inhibitor impairs parenchymal plaque development in an Alzheimer's disease model. Nat Commun. 2019;10(1):3758. 10.1038/s41467-019-11674-z . PubMed PMID: 31434879; PubMed Central PMCID: PMC6704256.
13. Asai H, Ikezu S, Tsunoda S, Medalla M, Luebke J, Haydar T, et al. Depletion of microglia and inhibition of exosome synthesis halt tau propagation. Nat Neurosci. 2015;18(11):1584–93. 10.1038/nn.4132 . PubMed PMID: 26436904; PubMed Central PMCID: PMC4694577.
14. Leyns CEG, Ulrich JD, Finn MB, Stewart FR, Koscal LJ, Remolina Serrano J, et al. TREM2 deficiency attenuates neuroinflammation and protects against neurodegeneration in a mouse model of tauopathy. Proc Natl Acad Sci U S A. 2017;114(43):11524–9. 10.1073/pnas.1710311114 . PubMed PMID: 29073081; PubMed Central PMCID: PMC5663386.
15. Shi Y, Manis M, Long J, Wang K, Sullivan PM, Remolina Serrano J, et al. Microglia drive APOE-dependent neurodegeneration in a tauopathy mouse model. J Exp Med. 2019;216(11):2546–61. 10.1084/jem.20190980 . PubMed PMID: 31601677; PubMed Central PMCID: PMC6829593.

16. van Olst L, Simonton B, Edwards AJ, Forsyth AV, Boles J, Jamshidi P, et al. Microglial mechanisms drive amyloid-β clearance in immunized patients with Alzheimer's disease. Nat Med. 2025;31(5):1604–16. 10.1038/s41591-025-03574-1 . PubMed PMID: 40050704; PubMed Central PMCID: PMC12092304.
17. Albertini G, Zielonka M, Cuypers ML, Snellinx A, Xu C, Poovathingal S, et al. The Alzheimer's therapeutic Lecanemab attenuates Aβ pathology by inducing an amyloid-clearing program in microglia. Nat Neurosci. 2026;29(1):100–10. 10.1038/s41593-025-02125-8 . PubMed PMID: 41286448; PubMed Central PMCID: PMC12779577.
18. de Weerd L, Hummel S, Müller SA, Paris I, Sandmann T, Eichholtz M, et al. Early intervention anti-Aβ immunotherapy attenuates microglial activation without inducing exhaustion at residual plaques. Mol Neurodegener. 2025;20(1):92. 10.1186/s13024-025-00878-1 . PubMed PMID: 40830489; PubMed Central PMCID: PMC12366171.
19. Paolicelli RC, Sierra A, Stevens B, Tremblay ME, Aguzzi A, Ajami B, et al. Microglia states and nomenclature: A field at its crossroads. Neuron. 2022;110(21):3458–83. 10.1016/j.neuron.2022.10.020 . PubMed PMID: 36327895; PubMed Central PMCID: PMC9999291.
20. Keren-Shaul H, Spinrad A, Weiner A, Matcovitch-Natan O, Dvir-Szternfeld R, Ulland TK, et al. A Unique Microglia Type Associated with Restricting Development of Alzheimer's Disease. Cell. 2017;169(7):1276–e129017. 10.1016/j.cell.2017.05.018 . PubMed PMID: 28602351.
21. Leng F, Edison P. Neuroinflammation and microglial activation in Alzheimer disease: where do we go from here? Nat Rev Neurol. 2021;17(3):157–72. 10.1038/s41582-020-00435. -y PubMed PMID: 33318676.
22. Bouzid H, Belk JA, Jan M, Qi Y, Sarnowski C, Wirth S, et al. Clonal hematopoiesis is associated with protection from Alzheimer's disease. Nat Med. 2023;29(7):1662–70. 10.1038/s41591-023-02397-2 . PubMed PMID: 37322115; PubMed Central PMCID: PMC10353941.
23. Belk JA, Zhang Y, Shi Q, Ma L, Kalluru R, Enciso AM, et al. Somatic mutations reveal the ontogeny of human microglia. bioRxiv: Preprint Serv Biology. 2026. 10.64898/2026.05.19.726366 . PubMed PMID: 42239322; PubMed Central PMCID: PMC13228375.
24. Bennett ML, Bennett FC. The influence of environment and origin on brain resident macrophages and implications for therapy. Nat Neurosci. 2020;23(2):157–66. 10.1038/s41593-019-0545-6 . PubMed PMID: 31792468.
25. Aisenberg WH, O'Brien CA, Sangster M, Yaqoob F, Zhang Y, Temsamrit B, et al. Direct microglia replacement reveals pathologic and therapeutic contributions of brain macrophages to a monogenic neurological disease. Immunity. 2025;58(5):1254–e12689. 10.1016/j.immuni.2025.03.019 . PubMed PMID: 40311614; PubMed Central PMCID: PMC12078009.
26. Chadarevian JP, Lombroso SI, Peet GC, Hasselmann J, Tu C, Marzan DE, et al. Engineering an inhibitor-resistant human CSF1R variant for microglia replacement. J Exp Med. 2023;220(3):e20220857. 10.1084/jem.20220857 . PubMed PMID: 36584406; PubMed Central PMCID: PMC9814156.

27. Oakley H, Cole SL, Logan S, Maus E, Shao P, Craft J, et al. Intraneuronal beta-amyloid aggregates, neurodegeneration, and neuron loss in transgenic mice with five familial Alzheimer's disease mutations: potential factors in amyloid plaque formation. J Neurosci. 2006;26(40):10129–40. 2006 PubMed PMID: 17021169; PubMed Central PMCID: PMC6674618.
28. Chadarevian JP, Nguyen J, Le L, Ayala LA, Chadarevian AL, Zhou C, et al. CSF1R inhibitor-resistant model for CNS-wide microglia replacement strategies. Mol Ther. 2026;34(2):832–49. 10.1016/j.ymthe.2025.10.051 . PubMed PMID: 41232524; PubMed Central PMCID: PMC12882379.
29. Lombroso SI, Church EI, Anderson RN, O'Brien CA, Zhu Y, Dar AA, et al. Microglia replacement by peripheral delivery of CSF1R inhibitor-resistant hematopoietic cells. Mol Ther. 2026;34(2):850–66. 10.1016/j.ymthe.2025.10.050 . PubMed PMID: 41232525; PubMed Central PMCID: PMC12704446.
30. Wilkinson AC, Ishida R, Kikuchi M, Sudo K, Morita M, Crisostomo RV, et al. Long-term ex vivo haematopoietic-stem-cell expansion allows nonconditioned transplantation. Nature. 2019;571(7763):117–21. 10.1038/s41586-019-1244-x . PubMed PMID: 31142833; PubMed Central PMCID: PMC7006049.
31. Wilkinson AC, Ishida R, Nakauchi H, Yamazaki S. Long-term ex vivo expansion of mouse hematopoietic stem cells. Nat Protoc. 2020;15(2):628–48. 10.1038/s41596-019-0263-2 . PubMed PMID: 31915389; PubMed Central PMCID: PMC7206416.
32. Wang GG, Calvo KR, Pasillas MP, Sykes DB, Häcker H, Kamps MP. Quantitative production of macrophages or neutrophils ex vivo using conditional Hoxb8. Nat Methods. 2006;3(4):287–93. 10.1038/nmeth865 . PubMed PMID: 16554834.
33. Nemec KM, Uy G, Chaluvadi VS, Purnell FS, Elfayoumi B, Byerly L, et al. Microglia replacement by ER-Hoxb8 conditionally immortalized macrophages provides insight into Aicardi-Goutières syndrome neuropathology. Elife. 2026;14:RP102900. 10. 7554/eLife.102900 PubMed PMID: 41589671; PubMed Central PMCID: PMC12844908.
34. Forner S, Kawauchi S, Balderrama-Gutierrez G, Kramár EA, Matheos DP, Phan J, et al. Systematic phenotyping and characterization of the 5xFAD mouse model of Alzheimer's disease. Sci Data. 2021;8(1):270. 10.1038/s41597-021-01054-y . PubMed PMID: 34654824; PubMed Central PMCID: PMC8519958.
35. Bennett FC, Bennett ML, Yaqoob F, Mulinyawe SB, Grant GA, Hayden Gephart M, et al. A Combination of Ontogeny and CNS Environment Establishes Microglial Identity. Neuron. 2018;98(6):1170–e11838. 10.1016/j.neuron.2018.05.014 . PubMed PMID: 29861285; PubMed Central PMCID: PMC6023731.
36. O'Brien CA, Delcy SAS, Shukla S, Levitt EM, Cohen AS, Bennett ML, et al. Neonatal microglia replacement in mice modulates seizure severity in adulthood. Mol Ther. 2025;33(12):6248–64. 10.1016/j.ymthe.2025.08.039 . PubMed PMID: 40873033; PubMed Central PMCID: PMC12444772.
37. Liddelow SA, Guttenplan KA, Clarke LE, Bennett FC, Bohlen CJ, Schirmer L, et al. Neurotoxic reactive astrocytes are induced by activated microglia. Nature. 2017;541(7638):481–7. 10.1038/nature21029 . PubMed PMID: 28099414; PubMed Central PMCID: PMC5404890.

38. Foo LC. Purification and culture of astrocytes. Cold Spring Harb Protoc. 2013;2013(6):485–7. 10.1101/pdb.top. 070912 PubMed PMID: 23734014.

39. Marsh SE, Walker AJ, Kamath T, Dissing-Olesen L, Hammond TR, de Soysa TY, et al. Dissection of artifactual and confounding glial signatures by single-cell sequencing of mouse and human brain. Nat Neurosci. 2022;25(3):306–16. 10.1038/s41593-022-01022-8 . PubMed PMID: 35260865; PubMed Central PMCID: PMC11645269.

40. Zengeler KE, Hollis A, Deutsch TCJ, Samuels JD, Ennerfelt H, Moore KA, et al. Inflammasome signaling in astrocytes modulates hippocampal plasticity. Immunity. 2025;58(6):1519–e153511. 10.1016/j.immuni.2025.04.007 . PubMed PMID: 40318630; PubMed Central PMCID: PMC12158643.

41. Cronk JC, Filiano AJ, Louveau A, Marin I, Marsh R, Ji E, et al. Peripherally derived macrophages can engraft the brain independent of irradiation and maintain an identity distinct from microglia. J Exp Med. 2018;215(6):1627–47. 10.1084/jem.20180247 . PubMed PMID: 29643186; PubMed Central PMCID: PMC5987928.

42. Shemer A, Grozovski J, Tay TL, Tao J, Volaski A, Süß P, et al. Engrafted parenchymal brain macrophages differ from microglia in transcriptome, chromatin landscape and response to challenge. Nat Commun. 2018;9(1):5206. 10.1038/s41467-018-07548-5 . PubMed PMID: 30523248; PubMed Central PMCID: PMC6284018.

43. Bastos J, O'Brien C, Vara-Pérez M, Mampay M, van Olst L, Barry-Carroll L, et al. Monocytes can efficiently replace all brain macrophages and fetal liver monocytes can generate bona fide. SALL1 + microglia Immunity. 2025;58(5):1269–e128812. 10.1016/j.immuni.2025.04.006 . PubMed PMID: 40311613; PubMed Central PMCID: PMC12094688.

44. Bustamante J, Arias AA, Vogt G, Picard C, Galicia LB, Prando C, et al. Germline CYBB mutations that selectively affect macrophages in kindreds with X-linked predisposition to tuberculous mycobacterial disease. Nat Immunol. 2011;12(3):213–21. 10.1038/ni.1992 . PubMed PMID: 21278736; PubMed Central PMCID: PMC3097900.

45. Gays F, Aust JG, Reid DM, Falconer J, Toyama-Sorimachi N, Taylor PR, et al. Ly49B is expressed on multiple subpopulations of myeloid cells. J Immunol. 2006;177(9):5840–51. 10.4049/jimmunol.177. .9.5840 PubMed PMID: 17056508.

46. Deming Y, Filipello F, Cignarella F, Cantoni C, Hsu S, Mikesell R, et al. The MS4A gene cluster is a key modulator of soluble TREM2 and Alzheimer's disease risk. Sci Transl Med. 2019;11(505):eaau2291. 10.1126/scitranslmed.aau. 2291 PubMed PMID: 31413141; PubMed Central PMCID: PMC6697053.

47. Marschallinger J, Iram T, Zardeneta M, Lee SE, Lehallier B, Haney MS, et al. Lipid-droplet-accumulating microglia represent a dysfunctional and proinflammatory state in the aging brain. Nat Neurosci. 2020;23(2):194–208. 10.1038/s41593-019-0566-1 . PubMed PMID: 31959936; PubMed Central PMCID: PMC7595134.

48. Haney MS, Pálovics R, Munson CN, Long C, Johansson PK, Yip O, et al. APOE4/4 is linked to damaging lipid droplets in Alzheimer's disease microglia. Nature. 2024;628(8006):154–61. 10.1038/s41586-024-07185-7 . PubMed PMID: 38480892; PubMed Central PMCID: PMC10990924.

49. Krasemann S, Madore C, Cialic R, Baufeld C, Calcagno N, El Fatimy R, et al. The TREM2-APOE Pathway Drives the Transcriptional Phenotype of Dysfunctional Microglia in Neurodegenerative Diseases. Immunity. 2017;47(3):566–e5819. 10.1016/j.immuni.2017.08.008 . PubMed PMID: 28930663; PubMed Central PMCID: PMC5719893.
50. Nugent AA, Lin K, van Lengerich B, Lianoglou S, Przybyla L, Davis SS, et al. TREM2 Regulates Microglial Cholesterol Metabolism upon Chronic Phagocytic Challenge. Neuron. 2020;105(5):837–e8549. 10.1016/j.neuron. .2019.12.007 PubMed PMID: 31902528.
51. Silvin A, Uderhardt S, Piot C, Da Mesquita S, Yang K, Geirsdottir L, et al. Dual ontogeny of disease-associated microglia and disease inflammatory macrophages in aging and neurodegeneration. Immunity. 2022;55(8):1448–e14656. 10.1016/j.immuni.2022.07.004 . PubMed PMID: 35931085.
52. Hasel P, Rose IVL, Sadick JS, Kim RD, Liddelow SA. Neuroinflammatory astrocyte subtypes in the mouse brain. Nat Neurosci. 2021;24(10):1475–87. 10.1038/s41593-021-00905-6 . PubMed PMID: 34413515.
53. Batiuk MY, Martirosyan A, Wahis J, de Vin F, Marneffe C, Kusserow C, et al. Identification of region-specific astrocyte subtypes at single cell resolution. Nat Commun. 2020;11(1):1220. 10.1038/s41467-019-14198-8 . PubMed PMID: 32139688; PubMed Central PMCID: PMC7058027.
54. Chai H, Diaz-Castro B, Shigetomi E, Monte E, Octeau JC, Yu X, et al. Neural Circuit-Specialized Astrocytes: Transcriptomic, Proteomic, Morphological, and Functional Evidence. Neuron. 2017;95(3):531–e5499. 10.1016/j.neuron.2017.06.029 . PubMed PMID: 28712653; PubMed Central PMCID: PMC5811312.
55. Mizrak D, Levitin HM, Delgado AC, Crotet V, Yuan J, Chaker Z, et al. Single-Cell Analysis of Regional Differences in Adult V-SVZ Neural Stem Cell Lineages. Cell Rep. 2019;26(2):394–e4065. 10.1016/j.celrep.2018.12.044 . PubMed PMID: 30625322; PubMed Central PMCID: PMC6368857.
56. Phipson B, Sim CB, Porrello ER, Hewitt AW, Powell J, Oshlack A. propeller: testing for differences in cell type proportions in single cell data. Bioinformatics. 2022;38(20):4720–6. 10.1093/bioinformatics/btac582 . PubMed PMID: 36005887; PubMed Central PMCID: PMC9563678.
57. Marques S, Zeisel A, Codeluppi S, van Bruggen D, Mendanha Falcão A, Xiao L, et al. Oligodendrocyte heterogeneity in the mouse juvenile and adult central nervous system. Science. 2016;352(6291):1326–9. 10.1126/science.aaf6463 . PubMed PMID: 27284195; PubMed Central PMCID: PMC5221728.
58. Zeisel A, Hochgerner H, Lönnerberg P, Johnsson A, Memic F, van der Zwan J, et al. Molecular Architecture of the Mouse Nervous System. Cell. 2018;174(4):999–e101422. 10.1016/j.cell.2018.06.021 . PubMed PMID: 30096314; PubMed Central PMCID: PMC6086934.
59. Huang AY, Zhou Z, Talukdar M, Enyenihi L, Miller MB, Chhouk B, et al. Somatic cancer variants enriched in Alzheimer's disease microglia-like cells drive inflammatory and proliferative states. Cell. 2026;189(12):3719–e373524. 10.1016/j.cell.2026.03.040 . PubMed PMID: 42019491; PubMed Central PMCID: PMC13107304.

60. Nott A, Holtman IR, Coufal NG, Schlachetzki JCM, Yu M, Hu R, et al. Brain cell type-specific enhancer-promoter interactome maps and disease-risk association. Science. 2019;366(6469):1134–9. 10.1126/science.aay0793 . PubMed PMID: 31727856; PubMed Central PMCID: PMC7028213.
61. Prokop S, Miller KR, Drost N, Handrick S, Mathur V, Luo J, et al. Impact of peripheral myeloid cells on amyloid-β pathology in Alzheimer's disease-like mice. J Exp Med. 2015;212(11):1811–8. 10.1084/jem.20150479 . PubMed PMID: 26458768; PubMed Central PMCID: PMC4612091.
62. Varvel NH, Grathwohl SA, Degenhardt K, Resch C, Bosch A, Jucker M, et al. Replacement of brain-resident myeloid cells does not alter cerebral amyloid-β deposition in mouse models of Alzheimer's disease. J Exp Med. 2015;212(11):1803–9. 10.1084/jem.20150478 . PubMed PMID: 26458770; PubMed Central PMCID: PMC4612086.
63. Wu J, Wang Y, Li X, Ouyang P, Cai Y, He Y, et al. Microglia replacement halts the progression of microgliopathy in mice and humans. Science. 2025;389(6756):eadr1015. 10.1126/science.adr1015 . PubMed PMID: 40638739.
64. Sosna J, Philipp S, Albay R, Reyes-Ruiz JM, Baglietto-Vargas D, LaFerla FM, et al. Early long-term administration of the CSF1R inhibitor PLX3397 ablates microglia and reduces accumulation of intraneuronal amyloid, neuritic plaque deposition and pre-fibrillar oligomers in 5XFAD mouse model of Alzheimer's disease. Mol Neurodegener. 2018;13(1):11. 10.1186/s13024-018-0244-x . PubMed PMID: 29490706; PubMed Central PMCID: PMC5831225.
65. Baligács N, Albertini G, Borrie SC, Serneels L, Pridans C, Balusu S, et al. Homeostatic microglia initially seed and activated microglia later reshape amyloid plaques in Alzheimer's Disease. Nat Commun. 2024;15(1):10634. 10.1038/s41467-024-54779-w . PubMed PMID: 39639016; PubMed Central PMCID: PMC11621353.
66. Casali BT, MacPherson KP, Reed-Geaghan EG, Landreth GE. Microglia depletion rapidly and reversibly alters amyloid pathology by modification of plaque compaction and morphologies. Neurobiol Dis. 2020;142:104956. 10.1016/j.nbd.2020.104956 . PubMed PMID: 32479996; PubMed Central PMCID: PMC7526856.
67. Dodiya HB, Lutz HL, Weigle IQ, Patel P, Michalkiewicz J, Roman-Santiago CJ, et al. Gut microbiota-driven brain Aβ amyloidosis in mice requires microglia. J Exp Med. 2022;219(1):e20200895. 10.1084/jem.20200895 . PubMed PMID: 34854884; PubMed Central PMCID: PMC8647415.
68. Onos KD, Uyar A, Keezer KJ, Jackson HM, Preuss C, Acklin CJ, et al. Enhancing face validity of mouse models of Alzheimer's disease with natural genetic variation. PLoS Genet. 2019;15(5):e1008155. 10.1371/journal.pgen.1008155 . PubMed PMID: 31150388; PubMed Central PMCID: PMC6576791.
69. Wang J, Warden A, Xia B, Mostoller KE, Brandon B, Du M, et al. Global human myeloid replacement with peripheral progenitors induces interferonopathy and neurodegeneration. Res Square. 2025. 10.21203/rs.3.rs-7762822/v1 . PubMed PMID: 41256000; PubMed Central PMCID: PMC12622173.
70. Blurton-Jones M, Davtyan H, Chadarevian JP, Lakatos A, Lin S, Hasselmann J, et al. Brain wide engraftment of human monocytes induces neurodegeneration and cognitive dysfunction. Res

Square. 2025. 10.21203/rs.3.rs-7762816/v1 . PubMed PMID: 41282056; PubMed Central PMCID: PMC12632712.

71. Kim JS, Trzebanski S, Shin SH, Schori L, Frumer Friedman GR, Ilani NC, et al. Clonal hematopoiesis-associated motoric deficits caused by monocyte-derived microglia accumulating in aging mice. Cell Rep. 2025;44(5):115609. 10.1016/j.celrep.2025.115609 . PubMed PMID: 40279248.
72. Bennett ML, Bennett FC, Liddelow SA, Ajami B, Zamanian JL, Fernhoff NB, et al. New tools for studying microglia in the mouse and human CNS. Proc Natl Acad Sci U S A. 2016;113(12):E1738–1746. 10.1073/pnas.1525528113 . PubMed PMID: 26884166; PubMed Central PMCID: PMC4812770.
73. Tabula Muris Consortium, Overall coordination, Logistical coordination, Organ collection and processing, Library preparation and sequencing, Computational data analysis, et al. Single-cell transcriptomics of 20 mouse organs creates a Tabula Muris. Nature et al. 2018;562(7727):367–72. 10.1038/s41586-018-0590-4 PubMed PMID: 30283141; PubMed Central PMCID: PMC6642641.
74. Franzén O, Gan LM, Björkegren JLM. Database (Oxford). 2019. 10.1093/database/baz. 046 PubMed PMID: 30951143; PubMed Central PMCID: PMC6450036. PanglaoDB: a web server for exploration of mouse and human single-cell RNA sequencing data2019:baz046.
75. Hu C, Li T, Xu Y, Zhang X, Li F, Bai J, et al. CellMarker 2.0: an updated database of manually curated cell markers in human/mouse and web tools based on scRNA-seq data. Nucleic Acids Res. 2023;51(D1):D870–6. 10.1093/nar/gkac947 . PubMed PMID: 36300619; PubMed Central PMCID: PMC9825416.
76. Badia-I-Mompel P, Vélez Santiago J, Braunger J, Geiss C, Dimitrov D, Müller-Dott S, et al. decoupleR: ensemble of computational methods to infer biological activities from omics data. Bioinform Adv. 2022;2(1):vbac016. 10.1093/bioadv/vbac016 . PubMed PMID: 36699385; PubMed Central PMCID: PMC9710656.
77. Ritchie ME, Phipson B, Wu D, Hu Y, Law CW, Shi W, et al. limma powers differential expression analyses for RNA-sequencing and microarray studies. Nucleic Acids Res. 2015;43(7):e47. 10.1093/nar/gkv007 . PubMed PMID: 25605792; PubMed Central PMCID: PMC4402510.
78. Liberzon A, Birger C, Thorvaldsdóttir H, Ghandi M, Mesirov JP, Tamayo P. The Molecular Signatures Database (MSigDB) hallmark gene set collection. Cell Syst. 2015;1(6):417–25. 10.1016/j.cels.2015.12. .004 PubMed PMID: 26771021; PubMed Central PMCID: PMC4707969.
79. Pombo Antunes AR, Scheyltjens I, Lodi F, Messiaen J, Antoranz A, Duerinck J, et al. Single-cell profiling of myeloid cells in glioblastoma across species and disease stage reveals macrophage competition and specialization. Nat Neurosci. 2021;24(4):595–610. 10.1038/s41593-020-. 00789-y PubMed PMID: 33782623.
80. Christopherson KS, Ullian EM, Stokes CCA, Mullowney CE, Hell JW, Agah A, et al. Thrombospondins are astrocyte-secreted proteins that promote CNS synaptogenesis. Cell. 2005;120(3):421–33. 10.1016/j.cell. 2004.12.020 PubMed PMID: 15707899.

81. Allen NJ, Bennett ML, Foo LC, Wang GX, Chakraborty C, Smith SJ, et al. Astrocyte glypicans 4 and 6 promote formation of excitatory synapses via GluA1 AMPA receptors. Nature. 2012;486(7403):410–4. 10.1038/nature11059 . PubMed PMID: 22722203; PubMed Central PMCID: PMC3383085.
82. Blanco-Suarez E, Liu TF, Kopelevich A, Allen NJ. Astrocyte-Secreted Chordin-like 1 Drives Synapse Maturation and Limits Plasticity by Increasing Synaptic GluA2 AMPA Receptors. Neuron. 2018;100(5):1116–e113213. 10.1016/j.neuron.2018.09.043 . PubMed PMID: 30344043; PubMed Central PMCID: PMC6382071.
83. Kucukdereli H, Allen NJ, Lee AT, Feng A, Ozlu MI, Conatser LM, et al. Control of excitatory CNS synaptogenesis by astrocyte-secreted proteins Hevin and SPARC. Proc Natl Acad Sci U S A. 2011;108(32):E440–449. 10.1073/pnas.1104977108 . PubMed PMID: 21788491; PubMed Central PMCID: PMC3156217.

Figures

Figure 1

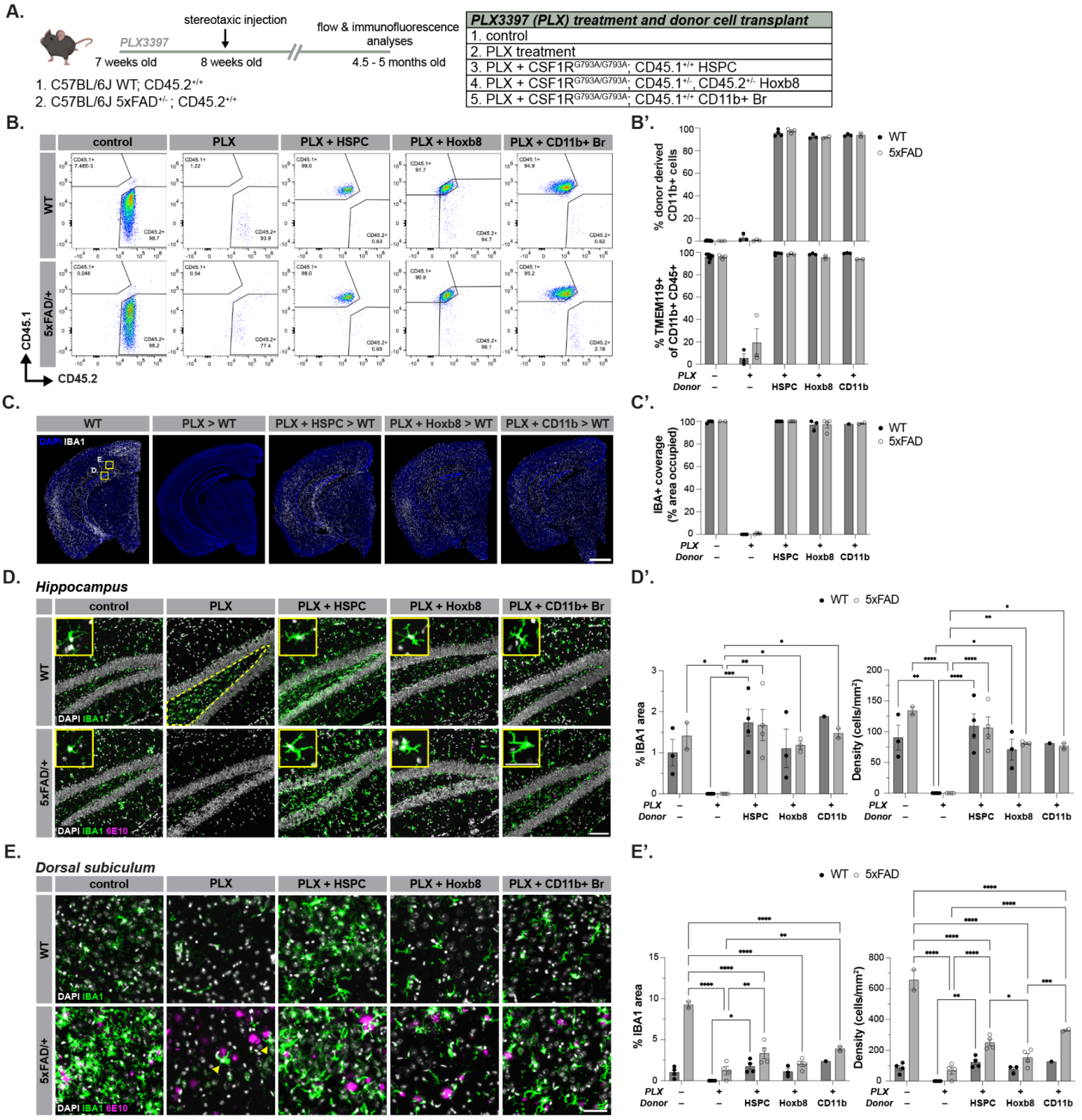

Figure 1

High efficiency microglia replacement in adult WT and 5xFAD mice using CSF1R inhibitor resistant donor cells.

(A) Transplantation schematic. C57BL/6J wild-type (WT; CD45.2$^{+/+}$) and C57BL/6J 5xFAD (5xFAD$^{+/-}$; CD45.2$^{+/+}$) mice were fed PLX3397 (PLX)-containing chow beginning at 7 weeks of age to deplete

endogenous microglia. At 8 weeks old, mice received stereotaxic intracranial injection of one of the following CSF1R^{G793A} expressing donor cell populations: hematopoietic stem and progenitor cells (HSPC, CD45.1$^{+/+}$), Hoxb8-immortalized myeloid progenitors (Hoxb8, CD45.1$^{+/-}$), or primary CD11b+ brain cells (CD11b+ Br, CD45.1$^{+/+}$). Untreated and PLX-only groups served as controls. Animals were harvested at 4.5–5 months of age for flow cytometry and immunofluorescence analyses.

(B) Representative plots showing CD45.1 vs. CD45.2 expression in CD11b+ cells from WT (top) and 5xFAD (bottom) mice across all five treatment conditions: no treatment, PLX alone, PLX + HSPC, PLX + Hoxb8, and PLX + CD11b+ brain cells. Cells were pre-gated on live/dead, size/granularity, singlets, and CD11b expression. Samples were acquired across multiple sessions, so donor and host gates were set independently for each acquisition using single-congenic control brains (CD45.1-only and CD45.2-only) run alongside the experimental samples on that day (**Figure S1A-C**). Plots are therefore comparable in gate assignment; absolute axis positions differ between sessions with instrument settings.

(B') Quantification of the percentage of CD45.1$^{+/+}$ (HSPC, primary CD11b+ brain cells) or CD45.1$^{+/-}$ (Hoxb8) cells among total CD11b+ (top) and the percentage of TMEM119+ cells among CD11b+ CD45+ cells (bottom) in WT (filled circles) and 5xFAD (open circles) mice across conditions. Data are mean ± SEM; n = 2-7 mice per group. Statistical comparisons by two-way ANOVA with Tukey's multiple comparisons post-hoc test. For CD11b/CD45 plot, untreated and PLX treated controls are significantly different (****$p < 0.0001$) from all three transplanted groups for comparisons made within each genotype. There were no significant differences when comparing WT and 5xFAD. For Tmem119 plot, PLX treated control is significantly different (****$p < 0.0001$) from untreated control and all three transplanted groups for comparisons made within each genotype. There were no significant differences when comparing WT and 5xFAD.

(C) Representative whole-brain coronal section immunofluorescence images showing IBA1+ cell dot renderings (gray) and DAPI (blue) across treatment conditions in WT mice. Scale bar, 1 mm. Boxes outline regions shown at higher magnification in subsequent panels.

(C') Quantification of IBA1+ coverage (% brain area containing IBA1+ cells) from whole-brain coronal sections in WT (filled circles) and 5xFAD (open circles) mice across conditions. Data are mean ± SEM; n = 1-4 mice per group. Statistical comparisons by two-way ANOVA with Tukey's multiple comparisons post-hoc test. PLX treated control is significantly different (****$p < 0.0001$) from untreated control and all three transplanted groups for comparisons made within each genotype.

(D) Representative immunofluorescence images of the hippocampus showing IBA1 (green) and DAPI (gray) in WT (top) and 5xFAD (bottom) mice across conditions. In 5xFAD sections, amyloid plaques are labeled with 6E10 (magenta). Yellow insets show individual IBA1+ cells at higher magnification. Scale bar, 100 μm. Inset scale bar, 50 μm. Yellow dotted line around the dentate gyrus outlining tissue background in PLX treated image.

(D') Quantification of IBA1+ area (% IBA1 area, top) and IBA1+ cell density (cells/mm², bottom) in the hippocampus of WT (filled circles) and 5xFAD (open circles) mice across conditions. Data are mean ± SEM; n = 1-4 mice per group. Statistical comparisons by two-way ANOVA with Tukey's multiple comparisons post-hoc test. *p < 0.05, **p < 0.01, ***p < 0.001, ****p < 0.0001.

(E) Representative immunofluorescence images of the dorsal subiculum showing IBA1 (green) and DAPI (gray) in WT (top) and 5xFAD (bottom) mice across conditions. In 5xFAD sections, amyloid plaques are labeled with 6E10. Scale bar, 100 μm. Yellow arrowheads pointing toward PLX persistent cells in PLX treated condition.

(E') Quantification of IBA1+ area (% IBA1 area, top) and IBA1+ cell density (cells/mm², bottom) in the dorsal subiculum of WT (filled circles) and 5xFAD (open circles) mice across conditions. Data are mean ± SEM; n = 1-4 mice per group. *p < 0.05, **p < 0.01, ***p < 0.001, ****p < 0.0001. Two-way ANOVA with Tukey's multiple comparisons post-hoc test.

Figure 2

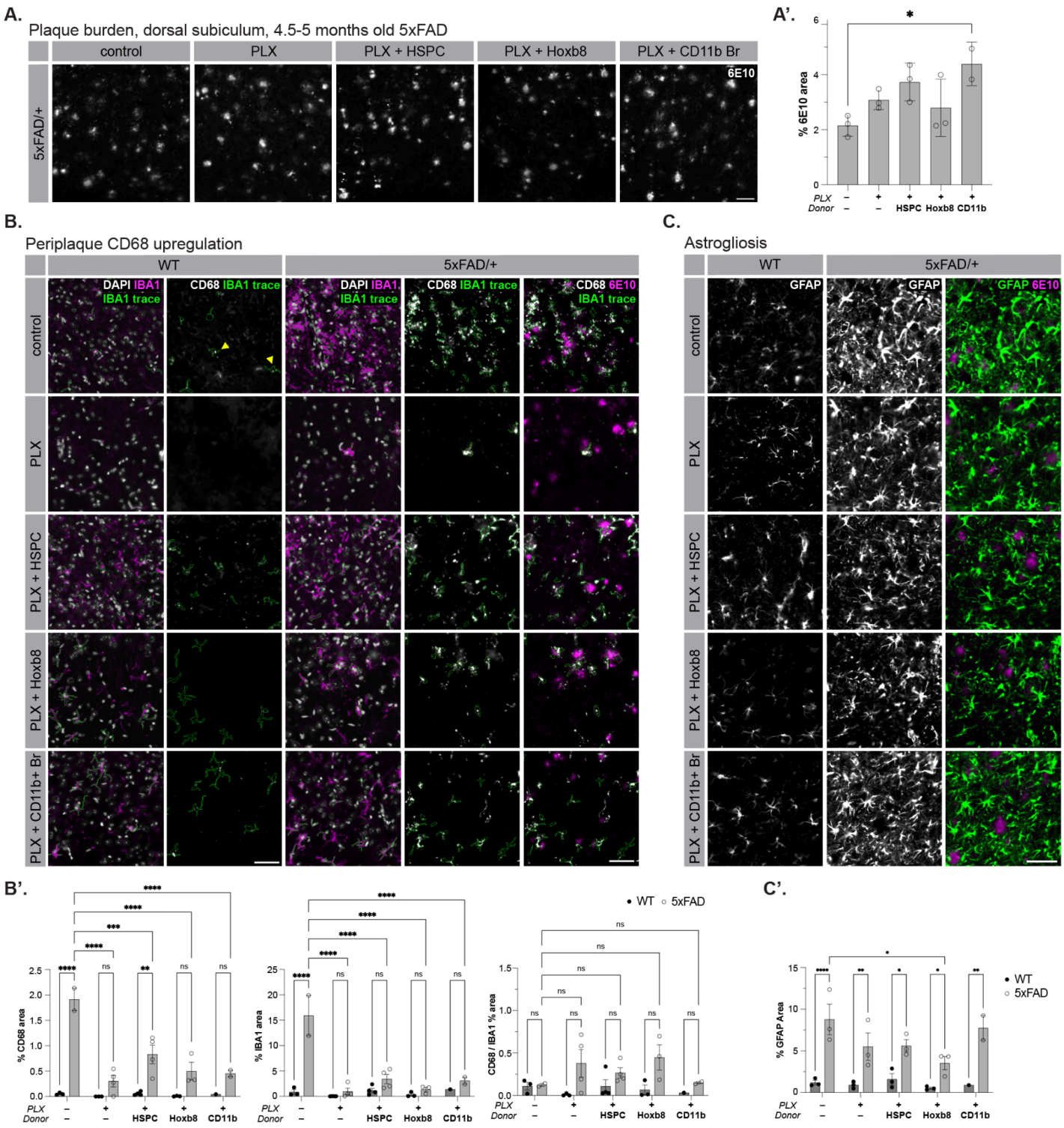

Figure 2

Plaque, CD68 and IBA1 immunofluorescence analysis in the dorsal subiculum of WT and 5xFAD mice across treatment conditions.

(A) Representative immunofluorescence images of the 5xFAD dorsal subiculum showing amyloid plaques labeled with 6E10 (white) across treatment conditions (control, PLX, PLX + HSPC, PLX + Hoxb8,

PLX + CD11b+ brain cells). Scale bar, 50 μm.

(A') Quantification of 6E10+ plaque area (% area) in the 5xFAD dorsal subiculum across treatment conditions. Data are mean ± SEM; n = 2-3 mice per group. Statistical comparisons by one-way ANOVA with Tukey's multiple comparisons post-hoc test. *p < 0.05.

(B) Representative immunofluorescence images of the dorsal subiculum from WT (left) and 5xFAD (right) mice across treatment conditions (control, PLX, PLX + HSPC, PLX + Hoxb8, PLX + CD11b+ brain cells). For WT tissues, the left panel displays a merged overlay of DAPI (gray), IBA1 (magenta), and IBA1 trace (green); the right panel shows CD68 (gray) merged with IBA1 trace (green). For 5xFAD tissues, the left panel displays a merged overlay of DAPI/IBA1/IBA1 trace; the middle panel displays a merged overlay of CD68 and IBA1 trace, while the bottom panel displays a merged overlay of CD68 (gray), IBA1 trace (green), and 6E10 (magenta). Scale bar, 50 μm.

(B') Quantification of % CD68 area (left), % IBA1 area (middle), and CD68/IBA1 % area (right) in the dorsal subiculum from WT (filled circles) and 5xFAD (open circles) mice across conditions. Data are mean ± SEM; n = 1-3 mice per group. Two-way ANOVA with Tukey's multiple comparisons post-hoc test was performed to test statistical significance. *p < 0.05, **p < 0.01, ****p < 0.0001; ns, not significant.

(C) Representative immunofluorescence images of the dorsal subiculum showing GFAP (gray) in WT (left row), 5xFAD (middle row), and 5xFAD with GFAP and 6E10 co-staining (GFAP in green, 6E10 in magenta; right row) across treatment conditions. Scale bar, 50 μm.

(C') Quantification of GFAP+ area (% GFAP area) in the dorsal subiculum across conditions in WT (filled circles) and 5xFAD (open circles) mice. Data are mean ± SEM; n = 1-3 mice per group. Statistical comparisons by two-way ANOVA with Šídák's multiple comparisons test. *p < 0.05, **p < 0.01; ****p < 0.0001.

Figure 3

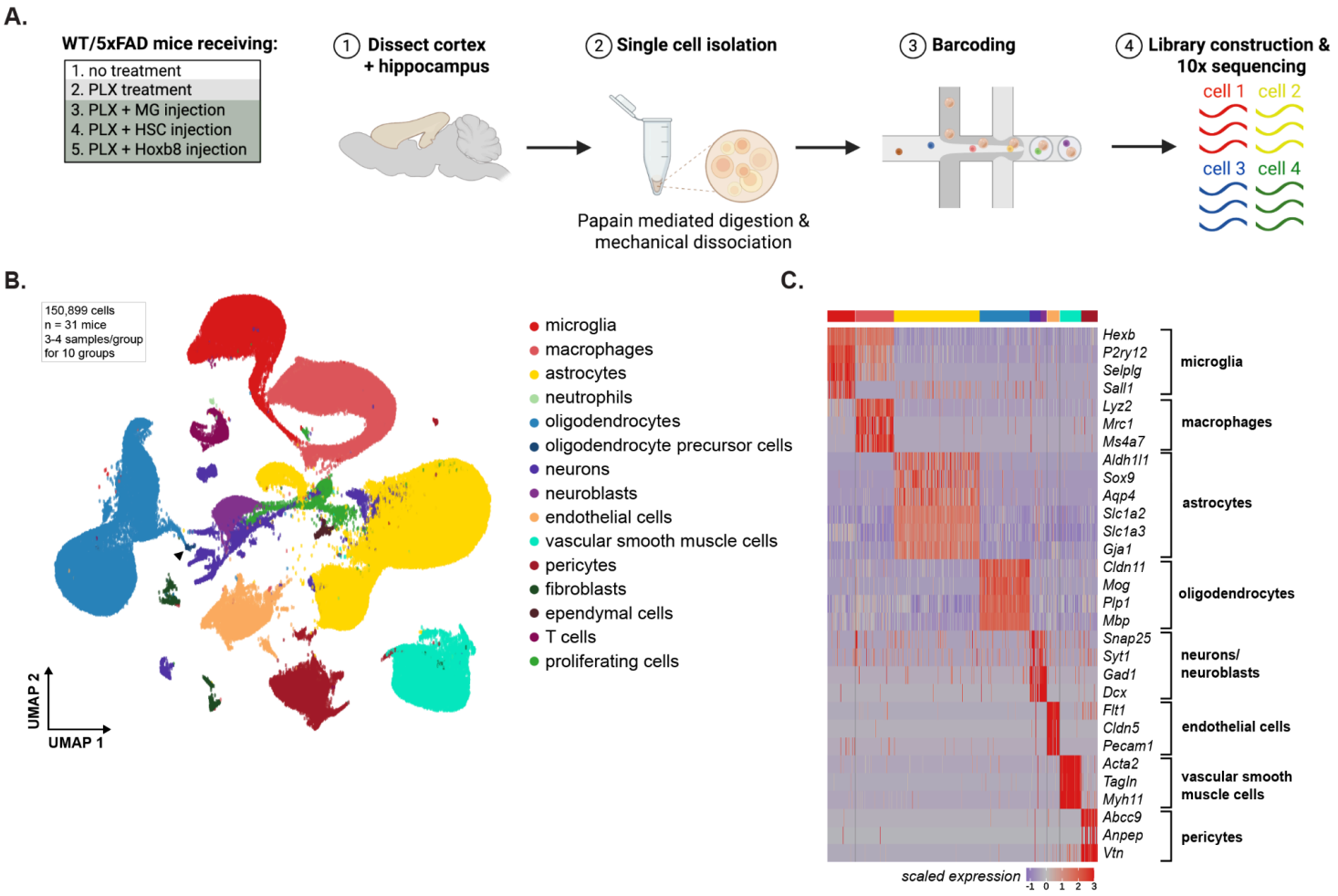

Figure 3

Single-cell transcriptomics of WT and 5xFAD brain across five microglia depletion and replacement conditions.

(A) Schematic of the scRNA-seq experimental workflow. Cortex and hippocampus of WT and 5xFAD mice from each of five treatment conditions (control, PLX, PLX + CD11b+ brain cells, PLX + HSPC, PLX + Hoxb8) were dissected, papain-digested, mechanically dissociated, and single-cell isolated. Barcoded cDNA library was constructed from single cell suspensions prior to Illumina sequencing.

(B) UMAP plot of resolved single cell profiles (150,899 cells from n=31 mice, 3-4 samples per group, from 10 experimental groups), colored and annotated by cell type: microglia, macrophages, astrocytes, neutrophils, oligodendrocytes, oligodendrocyte precursor cells, neurons, neuroblasts, endothelial cells, vascular smooth muscle cells, pericytes, fibroblasts, ependymal cells, T cells, and proliferating cells.

(C) Heatmap of scaled expression of canonical marker genes used for cell type annotation, including: microglia (*Hexb, P2ry12, Selplg, Sall1*); macrophages (*Lyz2, Mrc1, Ms4a7*); astrocytes (*Sox9, Aqp4, Slc1a2, Slc1a3, Gja1*); oligodendrocytes (*Cldn11, Mog, Plp1, Mbp*); neurons/neuroblasts (*Snap25, Syt1, Gad1, Dcx*);

endothelial cells (*Flt1, Cldn5, Pecam1*); vascular smooth muscle cells (Acta2, Tagln, Myh11); and pericytes (Abcc9, Anpep, Vtn).

Figure 4

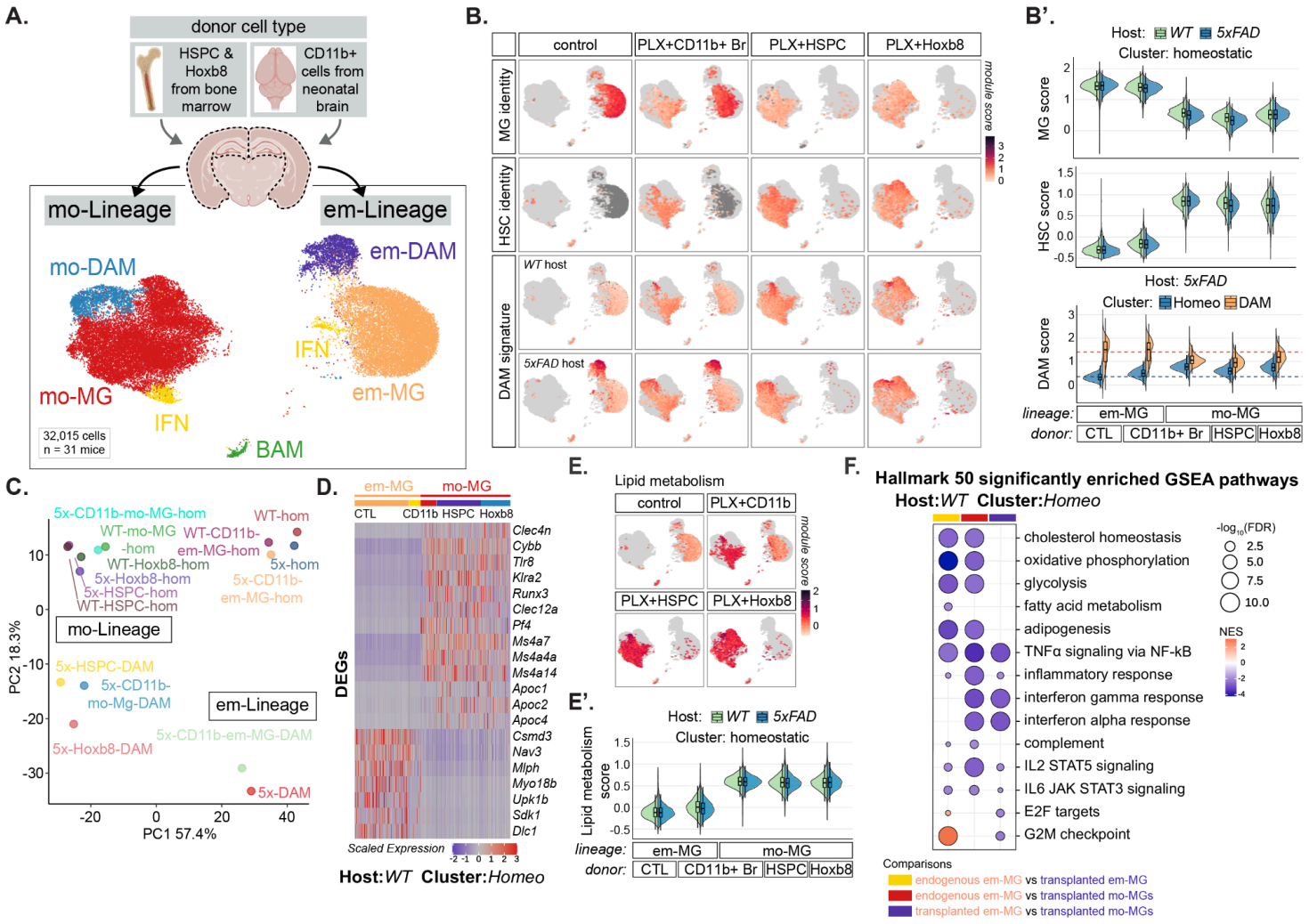

Figure 4

Single-cell RNAseq reveals shared and distinct features of Mo- and Em-MGs following microglia replacement in WT and 5xFAD hosts.

(A) UMAP plot of microglia/macrophages subclustered from all CNS UMAP (**Figure 3B**; 32,015 cells from n=31 mice). Six populations are annotated: homeostatic em-microglia (Em-MG), engrafted mo-microglia (Mo-MG), em-microglia DAMs (Mg-DAM), mo-microglia DAMs (Mo-DAM), interferon-responsive cells (IFR), and border-associated macrophages (BAM).

(B) Feature plots showing microglia identity (top row), HSC identity (2nd row), and DAM signature gene scores (3rd and 4th row) across treatment conditions (control, PLX + CD11b+ brain cells, PLX + Hoxb8, PLX + HSPC) in WT (top 3 rows) and 5xFAD hosts (row 4). Color scales reflect module score. Dark gray indicates module score below 0.

(B') Violin plots of microglia identity (top), HSC identity (middle), and DAM signature gene scores across microglia and macrophage populations. MG and HSC plots show homeostatic clusters, stratified by host animal genotype (WT: green; 5xFAD: blue). DAM plot is stratified by cluster in 5xFAD hosts (homeostatic: blue; DAM: orange; bottom plot).

(C) Principal component analysis (PCA) of pseudobulk transcriptomes from homeostatic and DAM subclusters across all conditions, plotting PC1 (accounting for 57.4% variance) against PC2 (accounting for 18.3% variance). Each data point represents expression of one subcluster (DAM, homeostatic) from each combination of host genotype and treatment condition. Each dot represents average expression of n = 3 biological replicates (individual replicates shown in **Figure S3E**).

(D) Notable differentially expressed genes between em- and mo-MGs in the homeostatic cluster of WT hosts. Heatmap represents scaled expression.

(E) Feature plots showing lipid metabolism module score across treatment conditions in WT hosts.

(E') Violin plots of lipid metabolism module score of homeostatic cells across treatment conditions and genotype (WT: green; 5xFAD: blue).

(F) GSEA dot plots comparing transplanted em-MG to endogenous em-MG, transplanted mo-MGs (pooled from all 3 mo-MG groups) to endogenous em-MG, and transplanted mo-MGs to transplanted em-MG in WT hosts. Dot size reflects -log10(adjusted p-value); dot color reflects the normalized enrichment score (NES). Positive NES indicates enrichment in either endogenous or transplanted em-MG (orange); negative NES indicates enrichment in transplanted em-MG or mo-MGs (purple). Adjusted p-value exceeding 0.05 is considered significant.

Figure 5

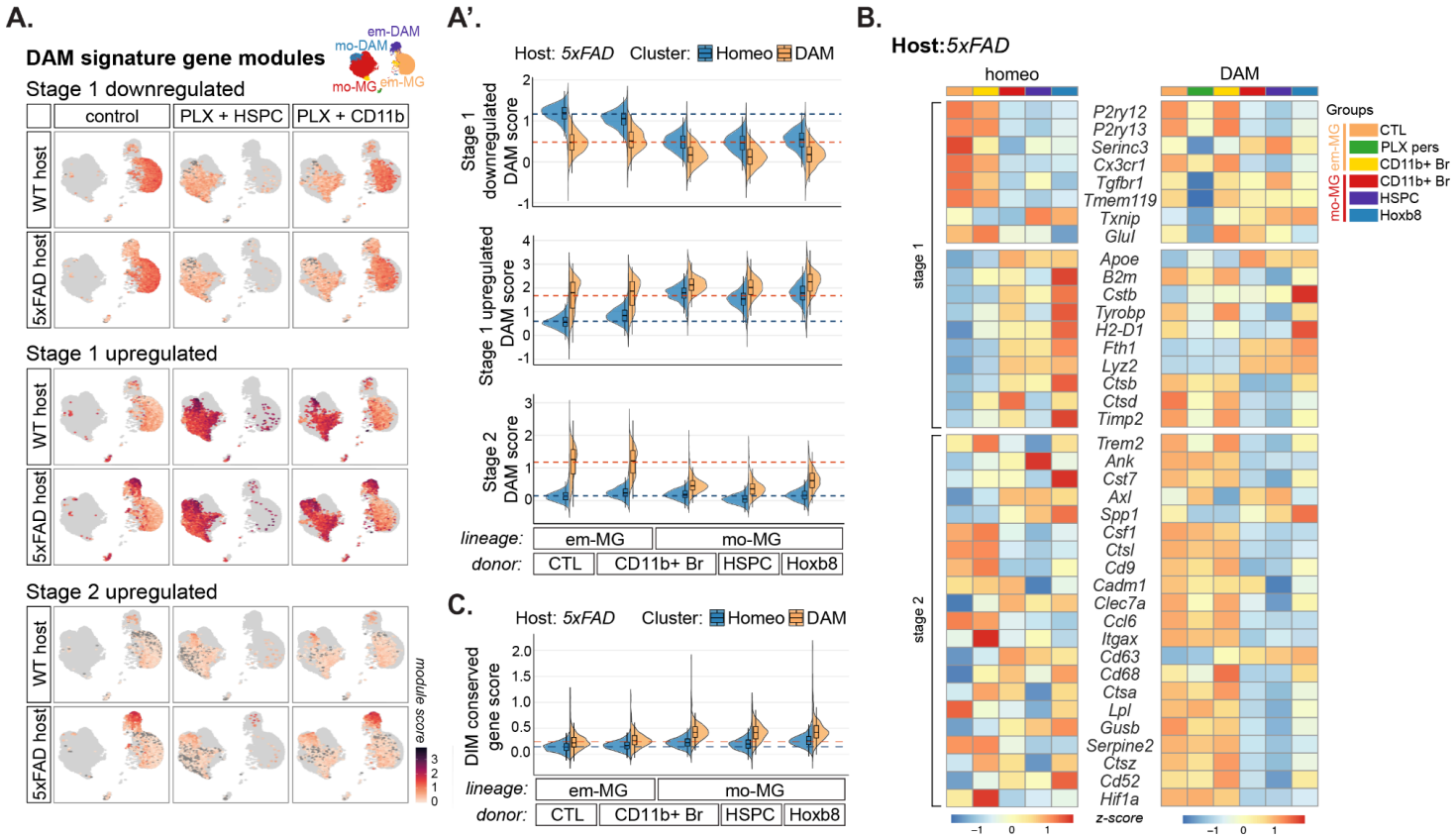

Figure 5

mo-MGs have altered regulation of DAM responses in the 5xFAD model

(A) Feature plots comparing functional module scores between mo- and em-MGs in WT and 5xFAD hosts. Top: stage 1 downregulated DAM gene module, consisting of microglial identity and surveillance genes. Middle: stage 1 upregulated DAM gene module, consisting of *Apoe*, lysosomal enzyme induction, innate immune activation, and antigen presentation genes. Bottom: stage 2 upregulated DAM gene module, consisting of lipid metabolism, lysosomal degradation, and phagocytosis genes. Color scale reflects module score. Dark gray indicates module score below 0.

(A') Violin plots of stage 1 downregulated gene set score (top), stage 1 upregulated gene set score (middle), and stage 2 upregulated gene set score (bottom) across treatment conditions and cell state (homeostatic: green; DAM: blue) in 5xFAD hosts.

(B) DAM signature genes in homeostatic and DAM clusters of 5xFAD hosts across control, PLX treated, and transplanted groups (from left to right for homeostatic cluster: endogenous em-MG, transplanted CD11b+ em-MG, transplanted CD11b+ mo-MG, HSPC-mo-MG, Hoxb8-mo-MG; from left to right for DAM cluster: endogenous em-DAM, PLX persistent em-DAM, transplanted CD11b+ em-DAM, transplanted CD11b+ mo-DAM, HSPC-mo-DAM, Hoxb8-mo-DAM). Color scale represents row z-score.

(C) Violin plots of DIM conserved gene set score by cluster, across treatment conditions, in 5xFAD hosts(homeostatic: green; DAM: blue).

Figure 6

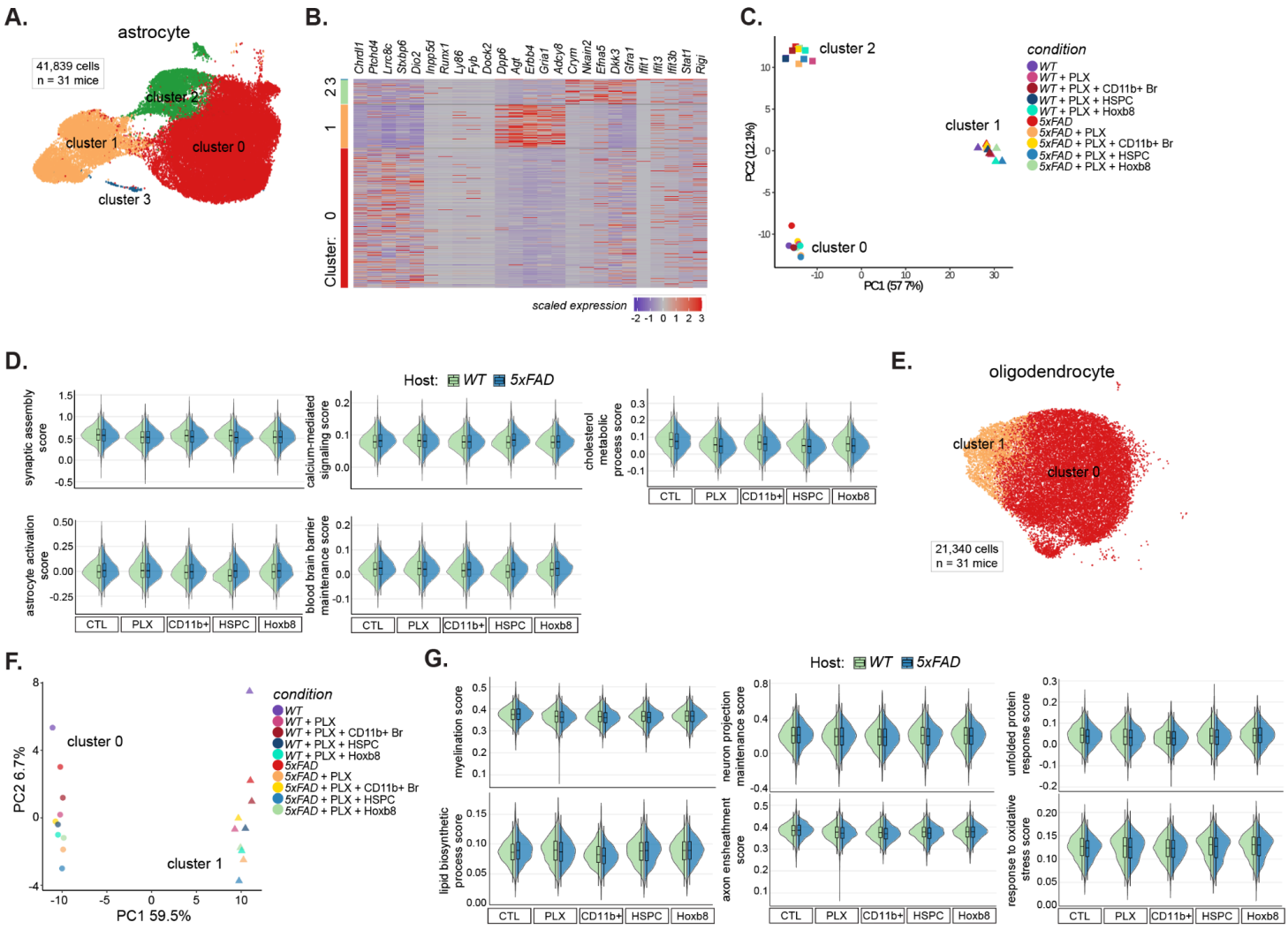

Figure 6

Transcriptional stability of astrocytes and oligodendrocytes following microglia depletion and replacement

(A) UMAP plot of astrocytes subclustered from all CNS UMAP (**Figure 3B**; 41,839 cells from n=31 mice), colored by clusters (0–3).

(B) Heatmap of scaled expression for the top marker genes enriched in each cluster using seurat's FindAllMarkers function.

(C) PCA of pseudobulk astrocyte transcriptomes across all conditions, with PC1 (accounting for 57.7% variance) plotted against PC2 (accounting for 12.1% variance). Points are colored by treatment condition and shaped by astrocyte clusters (0–2).

(D) Violin plots of astrocyte functional module scores across treatment conditions (control, PLX, PLX + CD11b+ brain cells, PLX + HSPC, PLX + Hoxb8) and genotypes (WT: green; 5xFAD: blue), including astrocyte activation, synaptic assembly, calcium-mediated synaptic signaling, cholesterol metabolic process, and blood brain barrier maintenance scores.

(E) UMAP projection of oligodendrocytes subclustered from all CNS UMAP (21,340 cells from n=31 mice), colored by clusters (0–1).

(F) PCA of pseudobulk oligodendrocyte transcriptomes across conditions, with PC1 (accounting for 59.5% variance) plotted against PC2 (accounting for 6.7% variance). Points are colored by treatment condition and shaped by clusters (0-1).

(G) Violin plots of oligodendrocyte functional module scores across treatment conditions (control, PLX, PLX + CD11b+ brain cells, PLX + HSPC, PLX + Hoxb8) and genotypes (WT: green; 5xFAD: blue), including myelination, lipid biosynthetic process, neuron projection maintenance, axon ensheathment, unfolded protein response, and response to oxidative stress scores.

Supplementary Files

This is a list of supplementary files associated with this preprint. Click to download.

- SUPPLEMENTARYFIGURELEGENDS.docx
- SupplementaryFigure6.png
- SupplementaryFigure4.png
- SupplementaryFigure1.png
- SupplementaryFigure5.png
- SupplementaryFigure3.png
- SupplementaryFigure2.png
- SupplementaryTable1.xlsx
- SupplementaryTable3.xlsx
- SupplementaryTable2.xlsx